Construction and Building Materials 414 (2024) 135058

Contents lists available at ScienceDirect

Construction and Building Materials

journal homepage: www.elsevier.com/locate/conbuildmat

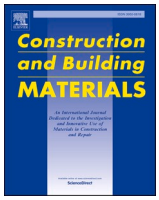

# Behaviour of reinforced concrete panels under impact loading after cryogenic freeze-thaw cycles

Kaiyi Chi, Jun Li *, Chengqing Wu *

*School of Civil and Environmental Engineering, University of Technology Sydney, NSW 2007, Australia*

ARTICLE INFO

*Keywords:*
Reinforced concrete panel
Impact load
Cryogenic freeze-thaw cycles
Numerical simulation

ABSTRACT

Concrete structures are widely used in modern constructions including energy storage system such as all concrete liquefied natural gas (ACLNG) storage tanks. In ACLNG tanks, concrete structure is exposed to cryogenic temperatures and freeze-thaw (FT) cycles. Cryogenic temperatures and FT cycles are recognized to influence the mechanical characteristics of concrete. To ensure safety of the critical energy infrastructure, it is crucial to explore the concrete structural response under the combined cryogenic FT cycles and accidental impact loading. This study aims to numerically examine the damage caused by impact loading on reinforced concrete panels after exposure to cryogenic FT cycles. A plasticity based continuous surface cap model was adopted to simulate concrete. The material modulus, uniaxial and triaxial strength surface as well as damage parameters were updated to incorporate the effect of cryogenic FT cycles. A numerical model was established to forecast the impact resistance of the reinforced concrete panels after various cryogenic FT cycles. Through the numerical simulation, it was evident that FT cycles exerted detrimental effects on the impact resistance of reinforced concrete panels. With an escalation in the number of FT cycles, there was a pronounced increase in the size of the crater formed on the top surface, accompanied by a corresponding rise in the penetration depth of the panel. The results of this research offer insights into the impact resistance of reinforced concrete structures following cryogenic FT cycles. Such insights are vital for the design and maintenance of critical structures like liquefied natural gas (LNG) storage tanks and other cryogenic facilities.

## 1. Introduction

Reinforced concrete structures play a vital role in various engineering applications, providing strength, durability, and resilience. However, when subjected to extreme environmental conditions, like cryogenic freeze-thaw (FT) cycles, the structural safety of concrete elements can be remarkably affected. Moreover, of specific concern is the accidental impact resistance of reinforced concrete structures while enduring the challenges posed by cryogenic FT cycles. The demand for efficient and reliable energy storage systems, particularly All Concrete LNG (ACLNG) storage tank, has been rapidly increasing in recent years [1,2]. Liquid natural gas storage tanks commonly maintain a storage temperature of approximately −165 °C, therefore, concrete is under ultra-low temperature condition. These storage tanks are subjected to both cryogenic temperatures, FT cycles and potential impact loading scenarios, rendering it crucial to assess their structural response and safety under such conditions.

Numerous researchers have investigated the concrete's mechanical properties at low and super-low temperatures to facilitate the scientific, rational, and cost-effective design of structures while ensuring their performance and safety in extreme cold environments [3–7]. Van de Veen [8] had a comprehensive review on the properties of concrete such as the compressive strength, tensile strength, modulus of elasticity at low and cryogenic temperature and after FT cycles. It revealed that the mechanical properties of concrete could be affected by the type of aggregate, cooling condition, water to cement ratio (w/c) and moisture content (MC). It is commonly reported that the strength of concrete was improved at low or super-low temperatures [1,8–10]. This improvement can be attributed to several factors. Firstly, as water within the concrete freezes at lower temperatures, it crystallizes into a solid reticulated pattern that imparts prestress to the concrete. This prestressing phenomenon contributes to an enhancement in the compressive strength due to the existence of multiaxial stress [6]. Moreover, the complete filling of capillary pores with ice helps eliminate stress concentrations within the concrete and inhibits the formation of microcracks at low temperatures. For a more comprehensive understanding of the reinforcement impacts of low temperatures on concrete, researchers have

* Corresponding authors.
*E-mail addresses:* Jun.Li-2@uts.edu.au (J. Li), Chengqing.Wu@uts.edu.au (C. Wu).

https://doi.org/10.1016/j.conbuildmat.2024.135058
Received 6 October 2023; Received in revised form 13 December 2023; Accepted 14 January 2024
Available online 20 January 2024

employed micro-scale models to explore the formation of ice within concrete pores and subsequent cracks [11,12].

On the other hand, the cryogenic FT cycles are recognized to lead to a deterioration in the mechanical properties of concrete. The deterioration is primarily attributed to the occurrence of FT damage, which arises from the repeated phase change of pore water within the concrete. Temperature fluctuations cause the pore water to either freeze or thaw, resulting in corresponding volume expansions or contractions. These volumetric changes exert stress on the microstructure of the concrete, ultimately inducing the formation of internal microcracks. With an increasing number of FT cycles, the cracks within the concrete widen and propagate, leading to cumulative damage to the overall structure. The progressive development of cracks weakens the integrity of the concrete and compromises its mechanical performance. The severity of FT damage is influenced by factors like the w/c ratio, the porosity of the concrete, and the number of FT cycles.

Over the last few decades, numerous scholars have explored the mechanical properties of concrete following cycles of low temperature FT exposure. A series of experiments regarding compressive and tensile strength as well as elastic modulus of concrete were conducted by Lee *et al.* [13] at a temperature range from 20 °C to − 70 °C both under monotonic and cyclic loadings. The study noted a slight reduction in compressive strength and elastic modulus after FT cycles. Rostásy and Punch [14] examined concrete compressive and splitting tensile strength at low temperatures varying from + 20 °C to − 170 °C, and they also tested residual strength after low temperature FT cycles between 20 °C and − 85 °C with a cooling rate of 1 ℃/min. It was reported that the higher water content in the concrete resulted in a loss of residual compressive strength up to 38% after 10 times FT cycles and the loss of tensile strength up to 57%. The concrete splitting tensile strength exhibited more prominent reductions after thermal cycles when compared to the compressive strength. Rostásy *et al.* [15] performed a series of experiment to explore the compressive and tensile strength of concrete after FT cycles with temperature ranged from 20 °C to − 30 °C, 20 °C to − 70 °C and 20 °C to − 170 °C, respectively. The findings revealed a gradual decline in the compressive strength of the concrete following each temperature cycle, with the majority of the damage occurring within the FT cycle from 20 °C to − 170 °C. Kim *et al.* [16] investigated both normal strength concrete (NSC) and ultra-high performance fibre reinforced concrete (UHPFRC) at cryogenic temperature (−170 °C) and 1 time of FT cycle. The results indicated the compressive and tensile strength for both materials increased significantly under cryogenic temperature, but slightly declined after 1 time FT cycle. Shi *et al.*[17–20] explored the compressive strength, tensile strength and elastic modulus of NSC after cryogenic FT cycles, the temperature ranged from 20 ℃ to − 120 ℃, − 30 ℃ to − 120 ℃, 10 ℃ to − 160 ℃ with cooling rate 1 ℃/min. With increased FT cycles, there was a notable cumulative influence of FT damage, resulting in a significant reduction in compressive strength, tensile strength and modulus of elasticity. They also adopted two FT methods to test the residual modulus of concrete. In Method 1, the FT cycle began from ambient temperature and in the Method 2, the FT cycle began from the low temperature limit. The results indicated that with the increase in the number of FT cycles, the elastic modulus of concrete using Method 1 decreased, while the elastic modulus of concrete using Method 2 remained unchanged or even slightly increased. This may be because the remarkable freezing effects of concrete pore water offset the cumulative effects of FT damage. Furthermore, uniaxial and triaxial compression tests were conducted by Zhou *et al.* [21] to evaluate the behaviour of high strength concrete and C60 after ultra-low temperature FT cycles between 20 °C to − 165 °C with cooling rate 2–3 ℃/min. The findings indicated that the strength of both high strength concrete and C60 concrete reduced as the number of ultra-low temperature FT cycles increased. The water–binder ratio (W/B) of C60 and high strength concrete was 0.27 and 0.21, respectively. Compared to C60, high strength concrete with a lower water cement ratio and smaller porosity showed a lower expansion strain. Therefore, the strength loss of high strength concrete after super-low temperature FT cycles was less. After 20 cycles of super-low temperature FT, the number of large and fine pores in the concrete increased significantly, leading to significant deterioration of the concrete structure. On the other hand, in accordance with Sun *et al.* [22], the Poisson's ratio of concrete exhibited relatively low sensitivity to the FT cycles.

Fracture energy is another important property that characterises the resistance of concrete against crack growth and failure, which represents the total energy that the concrete absorbs since the crack initiates. Ohlsson *et al.* [23] conducted three-point bending tests to understand the fracture energy and the fatigue strength of concrete across temperatures ranging from 20 °C to − 35 °C, using four different concrete grades: C25, C40, C45, and C100. Fatigue strength refers to the ability of a material to withstand repeated loading and unloading cycles without experiencing failure. It relates to the increased resistance of concrete to fatigue failure under low temperatures. The resistance is attributed to the mechanisms governing crack propagation during cyclic loading. Fatigue failures typically exhibit a more extensive pattern of cracks compared to static failures, resulting in a state where the material is more compromised or "cracked" after experiencing fatigue failure. A higher fracture energy and fatigue strength was observed at − 35 °C as compared to that at ambient temperature. Maturana *et al.*[24] employed three-point flexural tests to assess the fracture energy of concrete over a temperature range spanning from 20 °C to − 170 °C. It found out a remarkable rise in fracture energy as the temperature decreased. At − 170 °C, the fracture energy was roughly three times higher as compared to that at room temperature. Rocco *et al.* [25] investigated the fracture characteristics of concrete at 20, − 20, − 70, − 120 and − 170 °C, and conducted flexure bending and standard cylinder-splitting tests. It indicated that the reduction in the temperature resulted in an increase in fracture energy and splitting tensile strength owing to the freezing of water in the bulk of the concrete. However, there is a lack of research on the fracture energy of concrete after FT cycles. Xie *et al.* [26] studied the fracture energy of concrete after FT cycle in the range from 20 °C to − 80 °C via three-point bending tests. The findings indicated that as the lower temperature limit decreased and the number of cycles increased, the fundamental mechanical properties of concrete, along with the toughness of crack initiation and fracture energy, demonstrated a decreasing pattern.

While there has been extensive research focused on material performance at low temperatures or after FT cycle, limited attention has been given to reinforced concrete structures subjected to ultra-low temperatures and FT cycles. Some scholars have conducted experimental and numerical simulation studies on the bonding performance of reinforced concrete under ultra-low temperature and ultra-low temperature FT cycles. Vandewalle [27] used the pull-out test to explore the bonding behaviour between steel and concrete at 20, − 40, − 80, − 120 and − 165 °C. The results indicated the ultimate bond strength increased by 33.3%,77.8%, 100.0% and 94.4% at − 40, − 80, − 120 and − 165 °C, respectively, in comparison with the ultimate bond strength at ambient temperature. The ultimate bond strength increased with higher moisture content in the test piece. Jin *et al.* [28] and Zhang *et al.* [29] analysed the bond strength at cryogenic temperatures via numerical simulation and pull-out test. A linear increase of 11.8% in the ultimate bond strength was noted as the temperature decreased from 20 °C to − 120 °C. However, the residual bond strength and ultimate slip exhibited linear decline of 51.3% and 15.7%, respectively, while the bond strength reduces after FT cycles. Lee *et al.* [13] found out the bond strength declined by 1.1%, 2.5% and 8.5% after 1, 10 and 30 times of FT cycles at which temperature ranged from 20 °C to − 70 °C. Xie *et al.* [30] have conducted a pull-out test with temperature ranging from 20 ℃ to − 40 ℃, 20 ℃ to − 75 ℃ and 20 ℃ to − 120 ℃. As the number of cycles increases, the effect of each cycle on the reduction of bond strength gradually weakens. After three FT cycles, the average bond strength reduced by 6%, 13%, and 14% at FT temperatures of 20∼− 40 ℃,

20∼− 75 ℃, and 20∼− 120 ℃, respectively. The characteristics of concrete after FT cycles that mentioned in the introduction part are summarized in the Appendix.

Meanwhile some of the researchers investigated the flexure bending of reinforced structure at cryogenic temperatures. Liu et al. [31] employed four-point flexural bending tests on six reinforced concrete beams (with dimensions of 40 × 40 × 300 mm in width, height, and length, respectively) within a temperature range spanning from 20 °C to − 180 °C, which demonstrated that as the temperature decreased, there was an observable increase in both the load-bearing capacity as well as stiffness of the beams. The results indicated that the ultimate bearing capacity of the beams was significantly higher under low temperatures. Specifically, under the temperatures of − 40, − 80, − 120, − 160, and − 180 °C, the ultimate bearing capacity of the beams was amplified by 1.3, 1.4, 1.9, 2.1, and 2.6 times, respectively, as compared to the beam tested at ambient temperature. Nevertheless, the test beam sizes used in the previous studies were scaled proportionally, limiting the amount of information they could provide. Yan and Xie [32] conducted larger scale experiments to explore the performance of reinforced concrete beams at 20, − 40, − 70 and − 100 °C. They performed twelve groups of four-point flexural bending tests with reinforced concrete beams (65 × 120 × 1600 in terms of width, height, and length in mm). It indicated that the resistance of reinforced concrete beam improved at low temperature. The ultimate bearing capacity of the beams under the temperatures of − 40, − 70, and − 100 °C was 1.0 times, 1.1 times, and 1.3 times greater than the beam tested at ambient temperature, respectively.

Based on the above review, it is evident that exposure to low temperature FT cycles can lead to a decline in the mechanical properties of concrete. However, only limited study has been conducted on critical structure that suffers from ultra-low temperature and frequent FT cycles, and none of them is related with the impact resistance. The present study focuses on the impact resistance of reinforced concrete panels (the design was based on the dome in LNG storage tanks) after FT cycles. A numerical model was developed to analyse the impact behaviour of NSC panels subjected to FT cycles. The material constitutive model was modified to account for the changes in concrete performance resulting from FT cycles. A reinforced concrete panel model was then established to assess its impact resistance after various low-temperature FT cycles.

## 2. Constitutive models and material properties

### 2.1. CSCM concrete model

Continuous Surface Cap Model (CSCM) is a concrete material model used in LS-DYNA and other finite element analysis programmes. The nonlinear stress-strain response, failure mechanism, and overall

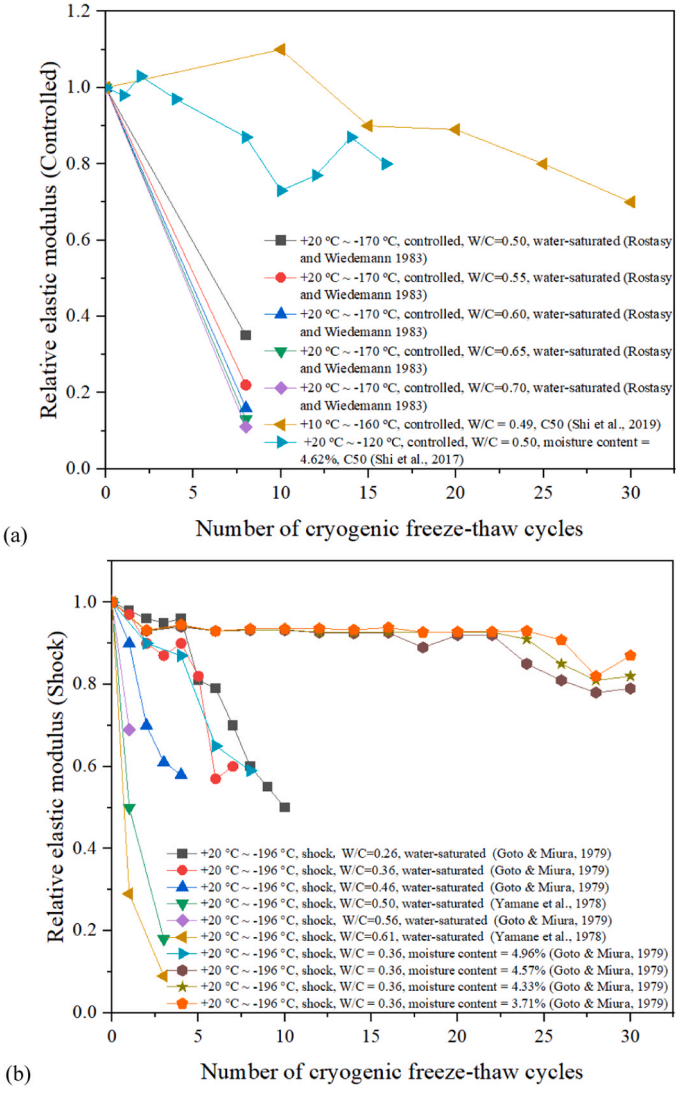


**Fig. 1.** Relative modulus of elasticity after various number of FT cycles. (a) Controlled (b) Thermal shock.

structural response of concrete under various load situations can be accurately simulated by the CSCM model. The CSCM model is available in two versions: MAT_CSCM and MAT_CSCM_CONCRETE. Three parameters need to input for MAT_CSCM_CONCRETE, of the concrete density ($\rho$), unconfined compressive strength ($f'_c$) and maximum aggregate size ($d_{max}$). According to CEB_FIP model code [33], the concrete density ($\rho$) is 2400 kg/m$^3$ for plain concrete and 2500 kg/m$^3$ for prestressed concrete. It is specifically designed for modelling normal strength concrete (NSC) with compressive strength between 28 to 58 MPa and the aggregate sizes between 8 and 32 mm [34]. In this particular study, to conduct simulation analysis on potential damage modes, MAT_CSCM_CONCRETE model is utilized to simulate normal strength concrete under room temperature conditions. It can generate parameters automatically by inputting $\rho$, $f'_c$ and $d_{max}$, which incorporate a set of standardised material properties, derived from laboratory test data, to serve as default material properties. However, the performance of concrete will change after cryogenic FT cycles, thus CSCM_ CONCRETE model cannot be simply used to generate parameters. MAT_CSCM model is employed to model normal strength concrete exposed to FT cycles, because it can update the parameter such as elastic modulus, compressive strength, fracture energy etc. after FT cycles. The subsequent section will delve into the critical parameters in detail.

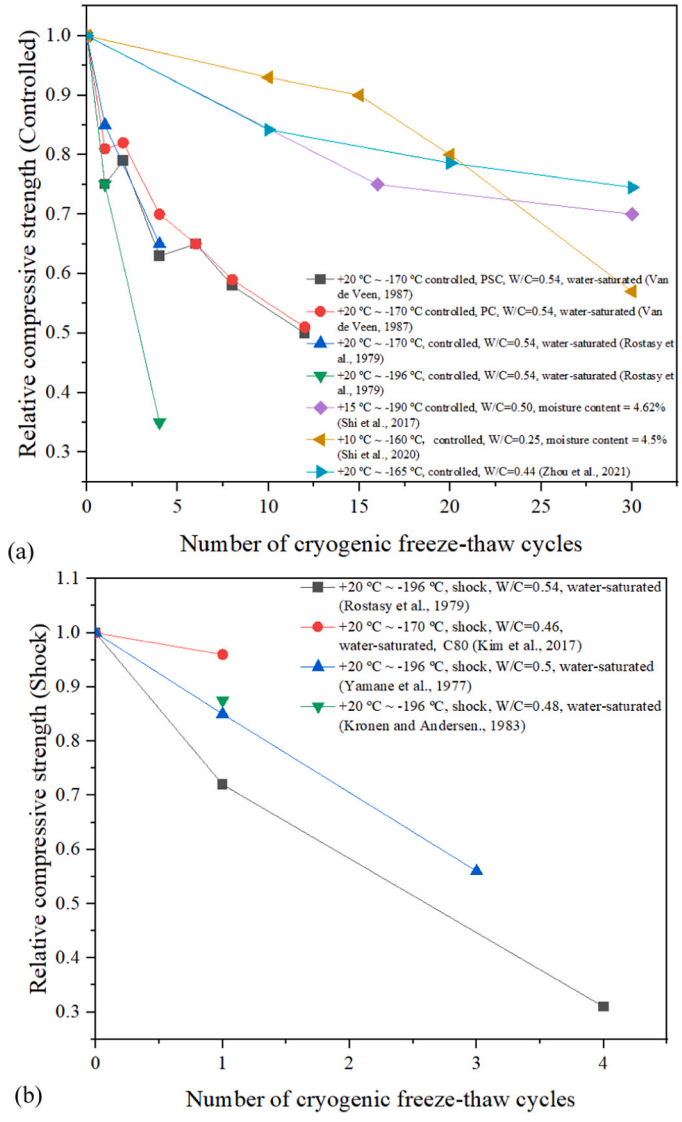


**Fig. 2.** Loss of compressive strength versus the number of thermal cycles. (a) Controlled (b) Thermal shock.

### 2.1.1. Shear modulus and bulk modulus after FT cycles

According to Goto and Miura [35], Yamane *et al.* [36], Rostásy and Wiedemann [37], Shi *et al.* [18] and Shi *et al.* [19], Fig. 1 summarises the loss of elastic modulus of NSC after different low-temperature FT cycles. It is noted that the loss of elastic modulus is related to a number of parameters such as the number of FT cycles, thermal loading, moisture content of concrete specimens, and water-to-cement ratio etc. For a particular concrete, with increased FT cycles, the loss of elastic modulus tends to increase. Based on the experiments conducted by Goto and Miura [35], Yamane *et al.* [36], when the water-to-cement (w/c) ratio and moisture content increased, a more rapid decrease in elastic modulus was observed [35]. Rostásy and Wiedemann [37] investigated the influence of a cooling rate on water-saturated concrete subjected to eight FT cycles. Their findings indicated that an increase in the w/c ratio caused a decline in elastic modulus. Generally, the influence on the internal structure of the concrete, characterized by the emergence of microcracks and the breakdown of the bond between cement paste and aggregates, contributed to a reduction in the elastic modulus following FT cycles. Besides, Fig. 1(b) demonstrates that, when subjected to identical cooling conditions, altering the w/c ratio results in a more significant reduction in the elastic modulus of concrete compared to changing the moisture content. Furthermore, shock conditions, such as immersing the concrete specimens in liquid nitrogen, resulting in a more pronounced influence on the elastic modulus of concrete. The intense forces generated during shock loading can result in microcracks and structural damage, leading to a substantial decrease in the elastic modulus.

### 2.1.2. Compressive strength after FT cycles

Similar to the elastic modulus, the compressive strength of concrete is influenced by diverse factors such as the number of FT cycles, moisture content, w/c ratio, and cooling techniques. Fig. 2 presents the experimental results conducted by different researcher [8,15,16,18,20,21,36,38], which demonstrates the effect of FT cycles on the concrete compressive strength. The data from these studies provide valuable insights into the relationship between FT cycles and the resulting compressive strength reduction in concrete. Most FT cycles range in temperature from room temperature to − 170 °C or − 196 °C, while FT cycle temperature range for Rostásy and Punch [14] is from room temperature to − 85 °C. The observation reveals that lowering the lower limit temperature of the FT cycle lead to a more evident reduction in the compressive strength. Fig. 2(b) provides a clear illustration that, when exposed to identical cooling conditions, a higher w/c ratio corresponds

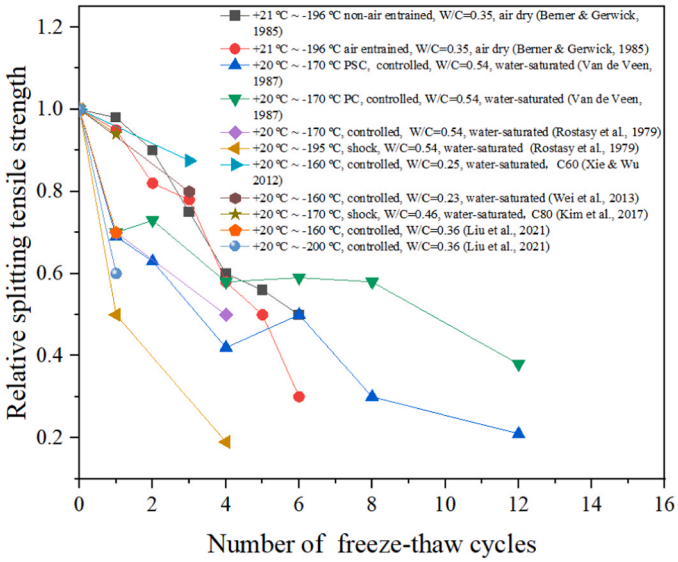


**Fig. 3.** Relative splitting tensile strength versus the number of thermal cycles.

to a more pronounced decrease in the relative compressive strength of concrete. Within a specific FT cycle range, using the same cooling method and w/c ratio, a higher moisture content in the concrete results in a greater decline in compressive strength under the same number of FT cycles. In accordance with the experimental results of Rostásy *et al.* [15], it can be deduced that the compressive strength experiences a more substantial reduction subjected to thermal shock as compared to controlled cooling. It implies that the application of shock cooling methods leads to a more rapid and pronounced decrease in the compressive strength.

#### 2.1.3. Splitting tensile strength after FT cycles

The number of FT cycles also influences the splitting tensile strength of concrete. Fig. 3 presents experimental data from various researchers [8,14–16,39–42], and reveals the changes in tensile strength of concrete after different FT cycles. It is observed that a decrease in the lower temperature limit in FT cycles causes a rise in the loss of splitting tensile strength. Furthermore, when saturated or highly moist concrete is exposed to sudden thermal shock, the decrease in splitting tensile strength is more significant as compared to slow cooling processes [37]. It should be emphasized that the splitting tensile strength demonstrates more remarkable reductions after thermal cycling as compared to the compressive strength.

#### 2.1.4. Damage parameters

Under low-pressure conditions, concrete or concrete-like materials demonstrate strain softening behaviour, which involves a decrease in strength after initial yielding. This behaviour is simulated using the damage algorithm within the CSCM model. There are five parameters need to be adjusted to capture the damage of concrete after FT cycles, including *B, GFC, D, GFT, GFS*. The parameter *B* specifically relates to the ductile shape softening behaviour, although limited attention has been paid to compressive softening behaviour despite numerous uniaxial compression tests being conducted. *GFC* represents fracture energy in uniaxial stress, *GFT* is fracture energy in uniaxial tension and *GFS* is fracture energy in pure shear stress. In the current study, the parameter *B* was assigned a default value of 100. In terms of parameter *D*, which governs brittle softening behaviour, a value of 0.001 was established following preliminary simulation attempts. For the parameter *GFS*, the user manual recommends setting it equal to *GFT* which is 100 times less than *GFC* [34]. The fracture parameter at ambient temperature was determined based on the guidelines provided by CEB-FIP [33] as follows,

$$G_f = G_{f0}\left(\frac{f_{CT}}{10}\right)^{0.7} \quad (1)$$

where $G_f$ represents the fracture energy in N•mm/mm$^2$, the initial fracture energy, $G_{f0}$, is influenced by the characteristics of the coarse aggregate used in the concrete, $f_{CT}$ is the compressive strength of the concrete cylinder in MPa. When the maximum aggregate size $d_{max}$ = 8 mm, $G_{f0}$ = 0.025 N•mm/mm$^2$. When $d_{max}$ = 16 mm, $G_{f0}$ = 0.030 N•mm/mm$^2$. When $d_{max}$ = 32 mm, $G_{f0}$ = 0.058 N•mm/mm$^2$.

Owing to limited study on testing the fracture energy on concrete after low-temperature FT cycles, this article predicts the fracture energy of concrete after FT cycles based on experiments conducted by Xie *et al.* [26]. The empirical formula is *Relative* $G_f = 0.69 + 0.31 \times \exp(-0.19 \times N)$, where N represents the number of FT cycles. The fracture energy calculations of NSC after 10, 20, and 30 FT cycles are summarized in Tables 1, 2, and 3, respectively.

### 2.2. Single element test analysis

Adhering to the outlined procedure, the current study formulated the CSCM material model for NSC under various FT cycles. Single element tests were performed prior to the impact tests.

In the present study, a specific type of concrete material was employed with a uniaxial compressive strength of 53.8 MPa and a w/c ratio of 0.44. This material was utilized to investigate the effects of FT cycles on concrete properties, drawing from Zhou's previous study [21]. The investigation from Zhou *et al.* included various tests on this concrete material, such as uniaxial and triaxial compression tests. The outcomes of these single element tests were compared to experimental data (strain-stress curve). According to Zhou *et al.* [21], the concrete specimen's temperature was subjected to controlled fluctuations, ranging from room temperature down to − 165 °C, with a controlled temperature change rate of 2–3 °C per minute and a total of 10, 20, and 30 FT cycles. The axial deformation loading rate for both uniaxial and triaxial compression tests was set at 0.02 mm/min. In the triaxial compression tests, a confining pressure of 20 MPa was applied. The experimental results of concrete for uniaxial compressive strength were 45.3, 42.3 and 40.1 MPa after 10, 20 and 30 FT cycles, respectively. The experimental results of concrete for triaxial compressive strength were 103.1, 90.2, 84.4 and 80.4 MPa after 0, 10, 20 and 30 FT cycles, respectively.

The shear modulus $G = \frac{E}{2(1+\nu)}$ and the bulk modulus $K = \frac{E}{3(1-2\nu)}$ where $E$ represents Young's modulus, and $\nu$ is Poisson's ratio. In current study, the Poisson's ratio is 0.2, and the Young's modulus after 10, 20 and 30 FT cycles can be obtained based on the strain-stress curve from Zhou *et al.* [21] experimental results in Fig. 6.

The tensile strength of concrete was calculated by equation $0.6\sqrt{f'_c} = 4.4$ MPa at room temperature (where $f'_c$ is the uniaxial compressive strength at 20 °C) in the current study from AS3600:2018 [43]. To enhance the accuracy of predicting the reduction in tensile strength following various FT cycles, an empirical equation has been formulated based on the data presented in Fig. 3 as follows,

**Table 1**
Material parameters for NSC under 10 times of FT cycles.

| Parameter | Value | Parameter | Value | Parameter | Value | Parameter | Value |
|---|---|---|---|---|---|---|---|
| $R_o$ (kg/m$^3$) | 2400 | *NPLOT* | 1 | *INCRE* | 0 | *IRATE* | 1 |
| ERODE | 0 | *RECOV* | 0 | *ITRETRC* | 0 | *PRED* | 0 |
| G (Pa) | 2.25E10 | *K* (Pa) | 2.76E10 | $N_H$ | 1 | $C_H$ | 0 |
| α (Pa) | 1.33E7 | θ (Pa$^{-1}$) | 0.35 | λ (Pa) | 1.051E7 | β (Pa$^{-1}$) | 1.939E-8 |
| $\alpha_1$ (Pa) | 0.7473 | $\theta_1$ (Pa$^{-1}$) | 5.96E-10 | $\lambda_1$ (Pa) | 0.17 | $\beta_1$ (Pa$^{-1}$) | 4.828E-8 |
| $\alpha_2$ (Pa) | 0.66 | $\theta_2$ (Pa$^{-1}$) | 7.17E-10 | $\lambda_2$ (Pa) | 0.16 | $\beta_2$ (Pa$^{-1}$) | 4.828E-8 |
| *R* | 5 | $X_D$ (Pa) | 1E8 | *W* | 0.05 | | |
| $D_1$ (Pa$^{-1}$) | 2.5E-10 | $D_2$ (Pa$^{-2}$) | 3.5E-19 | | | | |
| *B* | 100 | *GFC* (Pa*m) | 6934 | *D* | 0.001 | *GFT* (Pa*m) | 69.34 |
| *GFS* (Pa*m) | 69.34 | *PWRC* | 5 | *PWRT* | 1 | *PWOD* | 0 |
| $\eta_{oc}$ | 1.90E-4 | $N_c$ | 0.78 | $\eta_{ot}$ | 8.155E-5 | *Nt* | 0.48 |
| *OVERC* | 3.192E7 | *OVERT* | 3.192E7 | *SRATE* | 1 | *REPOW* | 1 |

**Table 2**
Material parameters for NSC under 20 times of FT cycles.

| Parameter | Value | Parameter | Value | Parameter | Value | Parameter | Value |
|---|---|---|---|---|---|---|---|
| $R_o$ (kg/m$^3$) | 2400 | *NPLOT* | 1 | *INCRE* | 0 | *IRATE* | 1 |
| ERODE | 0 | *RECOV* | 0 | *ITRETRC* | 0 | *PRED* | 0 |
| G (Pa) | 1.69E10 | *K* (Pa) | 2.08E10 | $N_H$ | 1 | $C_H$ | 0 |
| α (Pa) | 1.27E7 | θ (Pa$^{-1}$) | 0.34 | λ (Pa) | 1.051E7 | β (Pa$^{-1}$) | 1.929E-8 |
| $\alpha_1$ (Pa) | 0.7473 | $\theta_1$ (Pa$^{-1}$) | 7.47E-10 | $\lambda_1$ (Pa) | 0.17 | $\beta_1$ (Pa$^{-1}$) | 5.456E-8 |
| $\alpha_2$ (Pa) | 0.66 | $\theta_2$ (Pa$^{-1}$) | 9.0E-10 | $\lambda_2$ (Pa) | 0.16 | $\beta_2$ (Pa$^{-1}$) | 5.456E-8 |
| *R* | 5 | $X_D$ (Pa) | 1E8 | *W* | 0.05 | | |
| $D_1$ (Pa$^{-1}$) | 2.5E-10 | $D_2$ (Pa$^{-2}$) | 3.5E-19 | | | | |
| *B* | 100 | *GFC* (Pa*m) | 6164 | *D* | 0.001 | *GFT* (Pa*m) | 61.64 |
| *GFS* (Pa*m) | 61.64 | *PWRC* | 5 | *PWRT* | 1 | *PWOD* | 0 |
| $\eta_{oc}$ | 1.552E-4 | $N_c$ | 0.78 | $\eta_{ot}$ | 7.6E-5 | *Nt* | 0.48 |
| *OVERC* | 2.877E7 | *OVERT* | 2.877E7 | *SRATE* | 1 | *REPOW* | 1 |

**Table 3**
Material parameters for NSC under 30 times of FT cycles.

| Parameter | Value | Parameter | Value | Parameter | Value | Parameter | Value |
|---|---|---|---|---|---|---|---|
| $R_o$ (kg/m$^3$) | 2400 | *NPLOT* | 1 | *INCRE* | 0 | *IRATE* | 1 |
| ERODE | 0 | *RECOV* | 0 | *ITRETRC* | 0 | *PRED* | 0 |
| G (Pa) | 1.483E10 | *K* (Pa) | 1.82E10 | $N_H$ | 1 | $C_H$ | 0 |
| α (Pa) | 1.23E7 | θ (Pa$^{-1}$) | 0.33 | λ (Pa) | 1.051E7 | β (Pa$^{-1}$) | 1.929E-8 |
| $\alpha_1$ (Pa) | 0.7473 | $\theta_1$ (Pa$^{-1}$) | 8.176E-10 | $\lambda_1$ (Pa) | 0.17 | $\beta_1$ (Pa$^{-1}$) | 5.746E-8 |
| $\alpha_2$ (Pa) | 0.66 | $\theta_2$ (Pa$^{-1}$) | 9.862E-10 | $\lambda_2$ (Pa) | 0.16 | $\beta_2$ (Pa$^{-1}$) | 5.746E-8 |
| *R* | 5 | $X_D$ (Pa) | 1E8 | *W* | 0.05 | | |
| $D_1$ (Pa$^{-1}$) | 2.5E-10 | $D_2$ (Pa$^{-2}$) | 3.5E-19 | | | | |
| *B* | 100 | *GFC* (Pa*m) | 5876 | *D* | 0.001 | *GFT* (Pa*m) | 58.76 |
| *GFS* (Pa*m) | 58.76 | *PWRC* | 5 | *PWRT* | 1 | *PWOD* | 0 |
| $\eta_{oc}$ | 1.408E-4 | $N_c$ | 0.78 | $\eta_{ot}$ | 7.344E-5 | *Nt* | 0.48 |
| *OVERC* | 2.736E7 | *OVERT* | 2.736E7 | *SRATE* | 1 | *REPOW* | 1 |

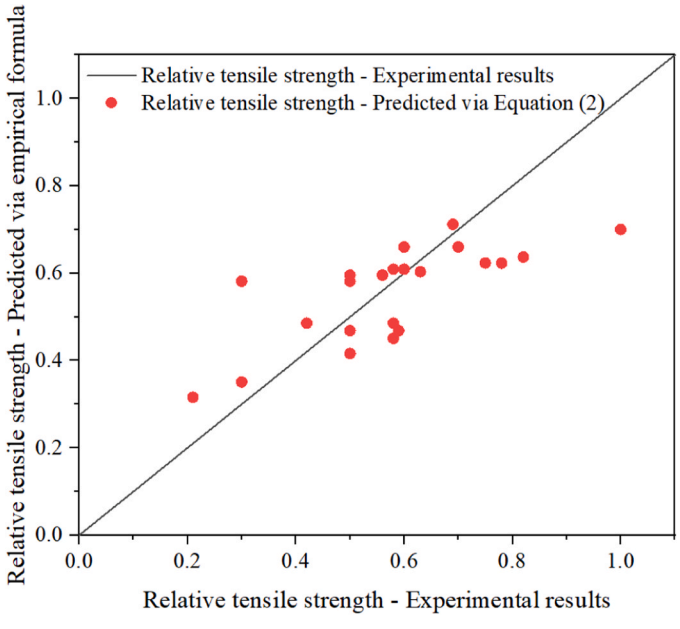


**Fig. 4.** Comparison of predicted relative tensile strength to experimental results.

$$\begin{aligned}\textit{Relative tensile strength} = {} & 0.70 + -2.36 \times 10^{-2} \times \mathrm{N} + -0.33 \\ & \times \left(\frac{\mathrm{W}}{\mathrm{c}}\right) + -1.58 \times 10^{-3} \times (\mathrm{MC}) + 2.79 \\ & \times 10^{-2} \times \mathrm{N} \times \left(\frac{\mathrm{W}}{\mathrm{c}}\right) + 1.18 \times 10^{-3} \times \mathrm{N} \\ & \times (\mathrm{MC}) + 8.24 \times 10^{-4} \times \left(\frac{\mathrm{W}}{\mathrm{c}}\right) \times (\mathrm{MC}) + -2.57 \\ & \times 10^{-3} \times \mathrm{N} \times \left(\frac{\mathrm{W}}{\mathrm{c}}\right) \times (\mathrm{MC}) \end{aligned} \quad (2)$$

where N represents to number of cycles, w/c is the ratio between water and cement and MC means moisture content of the concrete.

This equation represents the changes in tensile strength under controlled conditions. Fig. 4 below shows the comparison of the results between predicted formula and experimental data after cryogenic FT cycles. The coefficient of determination ($R^2$) for Eq. (2) is 0.85, indicating a good level of accuracy in predicting the tensile strength loss. Therefore, the predicted relative tensile strength formula can be utilised to investigate the tensile strength of concrete after various number of FT cycles. Based on the Eq. (2), it can be obtained that the relative tensile strength after 10, 20 and 30 FT cycles was 0.37, 0.30 and 0.24, respectively. According to the CSCM user's manual [34], the tensile strength $f'_t$ equals to $\frac{\alpha-\lambda}{\sqrt{3}}$.

In terms of the damage parameters, the value of *B* and *D* were 100 and 0.001 respectively as mentioned previously. In current study, the maximum aggregate size set as a default value 19 mm. Normally, the fracture energy parameter *GFC*, *GFT* and *GFS* can be automatically generated by inputting unconfined compressive strength in

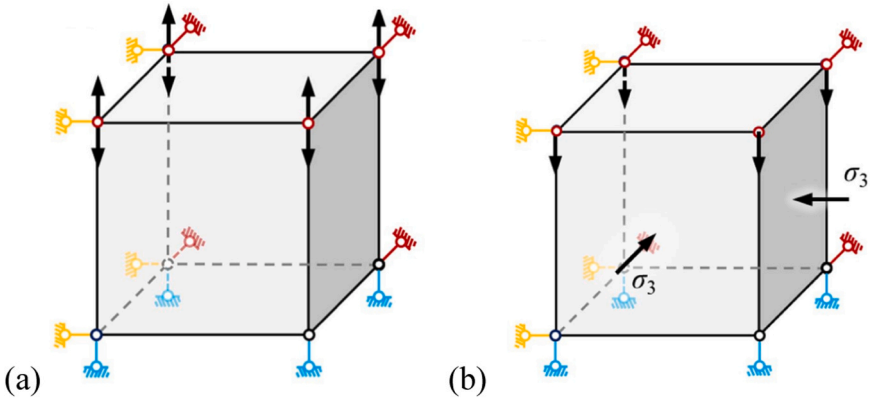


**Fig. 5.** Illustration of single element test: (a) unconfined uniaxial compression test, (b) triaxial compression test [44].

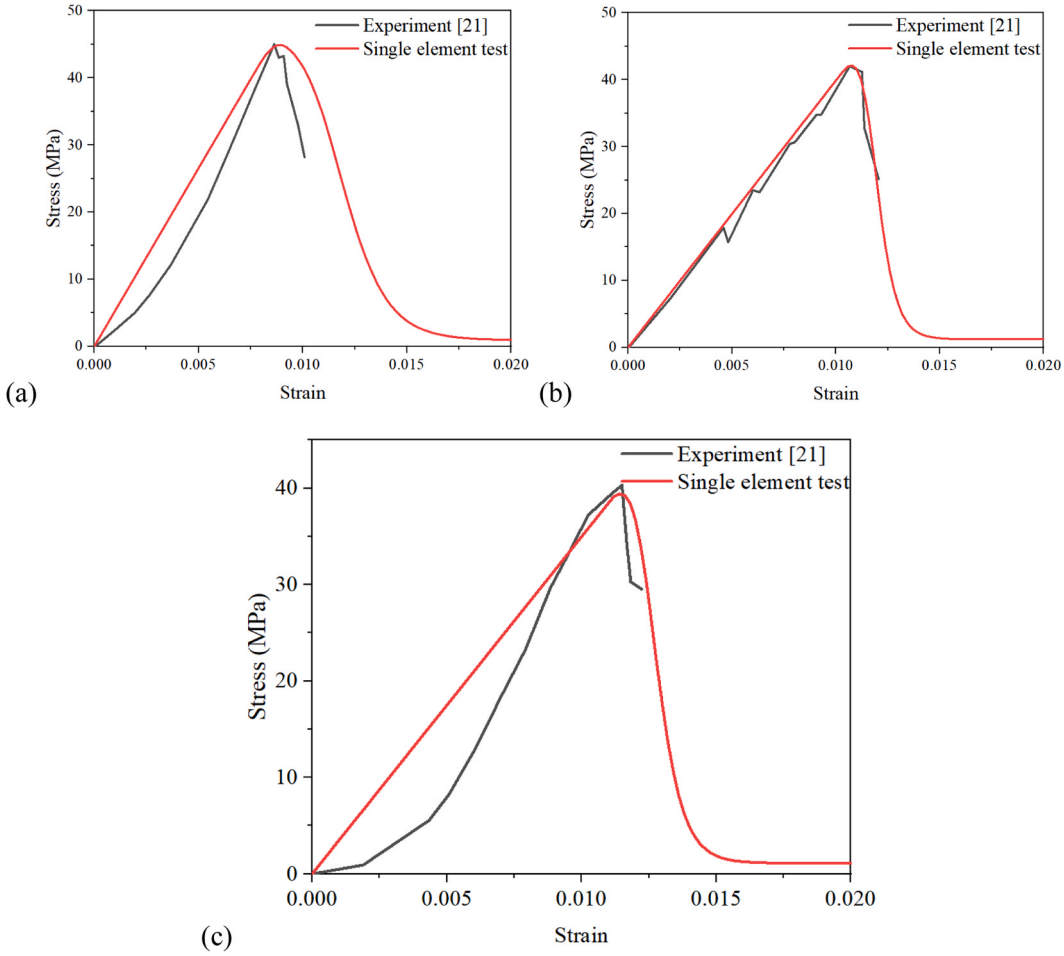


**Fig. 6.** Single model under uniaxial compression against different number of FT cycles (a) 10 times, (b) 20 times, (c) 30 times.

CSCM_CONCRETE model. When the unconfined compressive strength 45.3, 42.3 and 40.1 MPa after 10, 20 and 30 FT cycles were inputted, the value for *GFT* can be generated which is 93.7, 88.1 and 85.2, respectively. The relative fracture energy after 10, 20 and 30 times of FT cycles is 0.74, 0.70 and 0.69, respectively based on the empirical formula created in Section 2.1.4. Therefore, the value *GFT* can be updated by multiplying the relative fracture energy, which is 69.3, 61.6 and 58.8 respectively after 10, 20 and 30 times of FT cycles. As mentioned in Section 2.1.4, the value of *GFS* is equal to *GFT* and the value of *GFC* is 100 times greater than *GFT*. Tables 1,2 and 3 summarise the modified data for concrete after 10, 20 and 30 FT cycles.

In the single element tests, displacement control in unconfined uniaxial compression testing was achieved using the *PRESCRIBED_MOTION keyword, enabling precise control of the applied displacement (as depicted in Fig. 5(a)).

Confining pressure was exerted to four surfaces of the NSC model to simulate constraints during the triaxial compression test, while compressive load was applied by pushing down on the top surface. This configuration allowed for the simulation of triaxial compression conditions experienced by the NSC material (as illustrated in Fig. 5(b)).

Fig. 6 illustrates the stress-strain relationship of NSC under uniaxial compression after undergoing 10, 20, and 30 cycles of FT cycles. It can

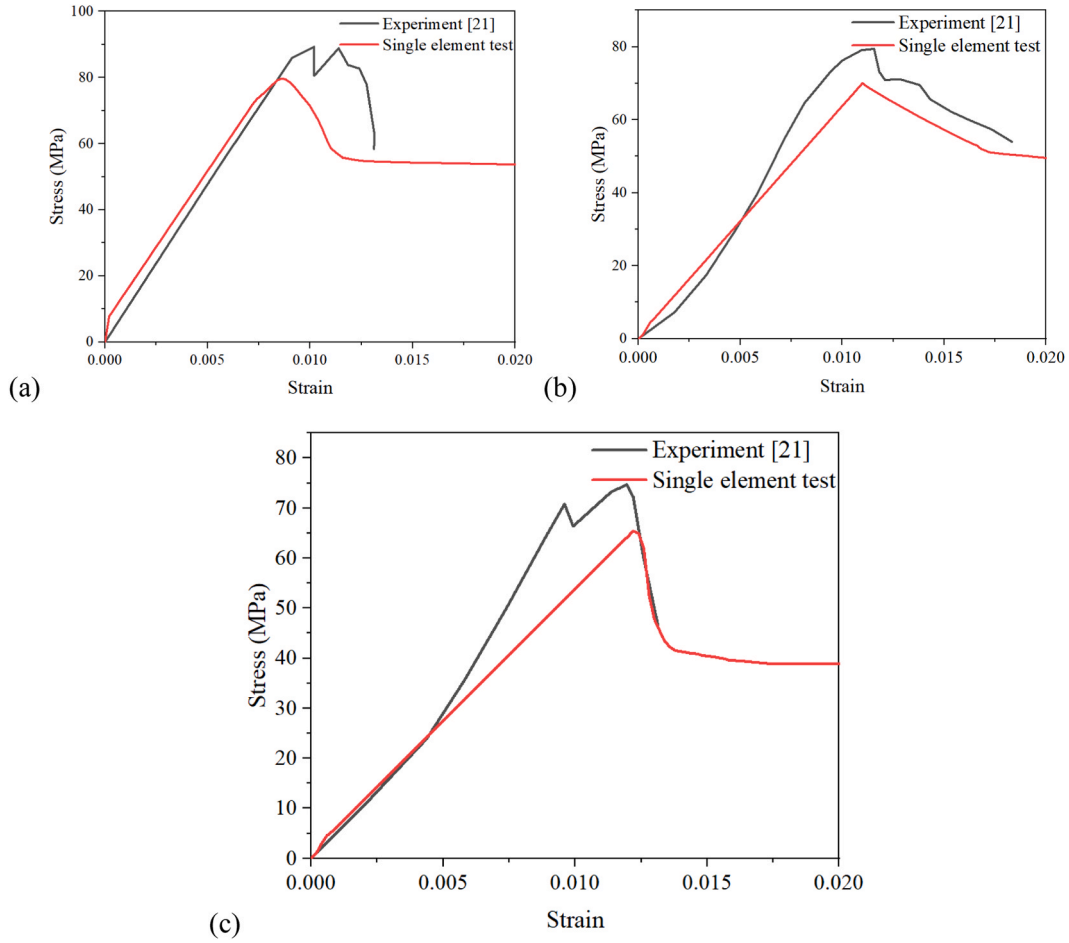


**Fig. 7.** Single model under triaxial compression against different number of FT cycles (a) 10 times, (b) 20 times, (c) 30 times.

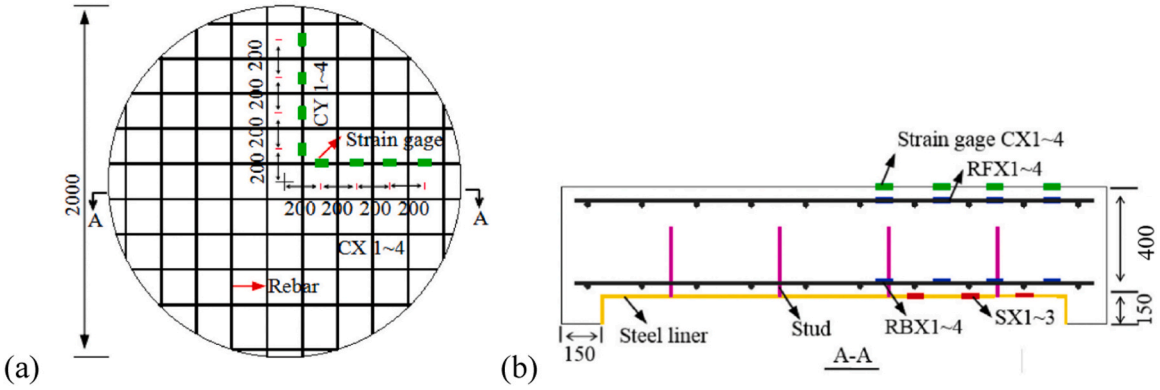


**Fig. 8.** Dimension of composite panel. (a) Front view (b) Side view (unit: mm) [49].

be clearly seen that the simulation result is in good agreement with the experimental results from Zhou *et al.* [21]. Tables 1, 2, and 3 provide a comprehensive summary of the CSCM parameters for NSC across varying numbers of FT cycles, derived from the experimental outcomes. Fig. 7 illustrates the stress–strain curve of NSC under triaxial compression after 10, 20 and 30 times of FT cycles. The error of ultimate strength was 10.47%. 11.75% and 11.92% compared with the experimental results after 10, 20 and 30 times of FT cycles, respectively. In the realm of numerical analysis concerning cementitious materials, forecasted errors below 20% are generally regarded as being within an acceptable range. However, it should be noted that the adjusted parameters within the CSCM model have a tendency to slightly underestimate material strength under elevated confining pressures [44]. Although the CSCM model exhibits satisfactory approximation to test data in cases without confinement, when it comes to high confinement scenarios, the numerical response becomes unstable to match even the peak strength observed in experimental data [45].

### 2.3. *Steel reinforcements model*

Steel bars possess different thermal properties as compared to the concrete matrix. They exhibit minimal dimensional changes under cryogenic conditions. This difference in thermal expansion and contraction properties between the reinforcement and the concrete

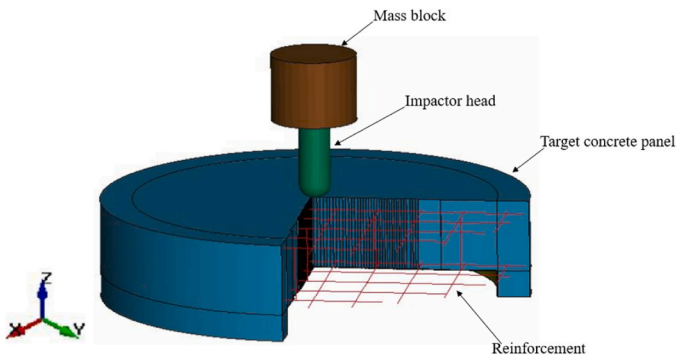


**Fig. 9.** Schematic view of impactor-panel system.

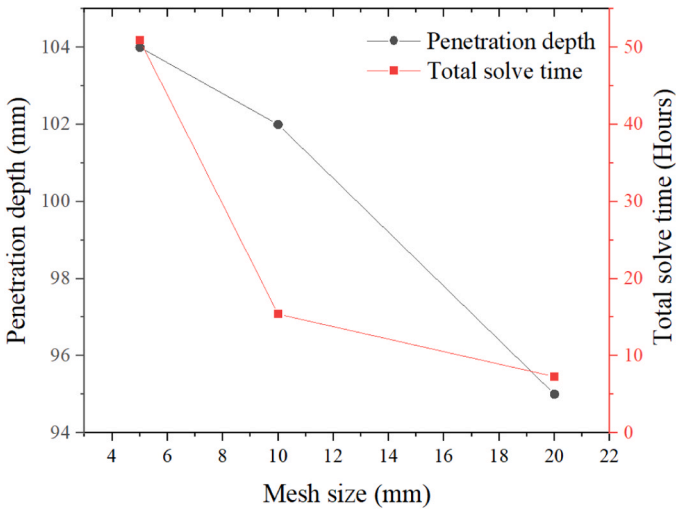


**Fig. 10.** Mesh convergence results of penetration depth.

matrix can provide some level of protection to the reinforcement. Yan and Xie [46] and Xie [47] conducted research on steel bars at low temperatures, and the results showed that the elastic modulus, tensile strength, and ultimate strength of the steel bars increased with the decrease of temperature. However, Jung et al. [48] stated that the fatigue failure of steel occurred after $10^4$ times load cycles under low temperature. The mechanical characteristics of steel reinforcements exhibit relatively consistent behaviour throughout the FT cycle exposures. The properties of steel bars after low-temperature FT cycling remained unchanged compared to those at room temperature, a conservative assumption made to guide the numerical simulation results in this study.

## 3. Validation of reinforced concrete panel under impact loadings

As mentioned previously, the safety and performance of many different structures at extremely low temperatures pose challenges, especially for liquefied natural gas storage tanks. This study aims to validate the impact resistance of the reinforced concrete/steel liner composite panels at ambient temperature, inspired by the design of the dome in LNG storage tanks, using the experimental data conducted by Zou *et al.* [49]. The composite target consisted of four parts, including concrete, reinforcements, studs and steel liner. As shown Fig. 8, the diameter of the panel was 2000 mm. There were two layers of reinforcements with 20 mm @ 200 mm. In addition, eight studs were contained in the target panel where four were arranged along 300 mm radius of the panel and the other were arranged along 700 mm, and the diameter of these studs was 12 mm. The 3 mm thick steel liner was welded at the bottom of the concrete panel. More details on the dimensions of target panel can be found in Zou et al. [49]. To access the impact resistance of concrete panel, a full numerical model was established using LS-DYNA. The numerical model of impactor and target panel is presented in Fig. 9. The impactor consisted of two parts: mass block and impactor head (100 kg). The radius of smooth spherical head for impactor head was 75 mm, and the height of cylindrical body was 375 mm.

In this study, two specimens were evaluated in comparison with the experimental outcomes. The first specimen was tested with 500 kg impactor at dropping height 35 m, and the impact velocity was 26.19 m/s. The second specimen was tested with 800 kg impactor and the falling height was 25 m (impact velocity was 22.13 m/s). The INITIAL_VELOCITY_GENERATION function in LS-DYNA was employed to achieve the desired impact velocity during the experiments. Three groups of mesh convergence tests have been done, including 5 mm, 10 mm and 20 mm mesh size for concrete, reinforcements, studs, steel liner and impactor. To balance the computational effort and accuracy, the mesh size of concrete, reinforcements, studs, steel liner and impactor was 10 mm (see Fig. 10).

MAT_CSCM_CONCRETE was utilised for concrete with density 2400 kg/m$^3$, 43.2 MPa compressive strength and 19 mm aggregate. MAT_PIECEWISE_LINEAR_PLASTICITY was adopted for studs and reinforcements in the model. MAT_PLASTIC_KINEMATIC was utilized for the steel liner material. The material model for both impactor head and

**Table 4**
Parameters of impactor-panel system.

| Material | LS-DYNA Model | Input Parameters | Magnitude |
|---|---|---|---|
| Concrete | MAT_CSCM_CONCRETE | Mass Density<br>NPLOT<br>Compression strength<br>Maximum aggregate | 2400 kg/m$^3$ 1<br>43.2 MPa<br>19 mm |
| Steel reinforcement/Stud | MAT_PIECEWISE_<br>LINEAR_PLASTICITY | Mass density<br>Yield strength<br>Poisson's ratio<br>Young's modulus | 7850 kg/m$^3$ 455 MPa<br>0.3<br>210 GPa |
| Steel liner | MAT_PLASTIC_KINEMATIC | Mass density<br>Yield strength<br>Poisson's ratio<br>Young's modulus | 7850 kg/m$^3$ 460 MPa<br>0.3<br>210 GPa |
| Impact head | MAT_RIGID | Mass density<br>Poisson's ratio<br>Young's modulus | 7850 kg/m$^3$ 0.22<br>117 GPa |
| Mass block | MAT_RIGID | Mass density<br>Poisson's ratio<br>Young's modulus | 7850 kg/m$^3$ 0.3<br>210 GPa |

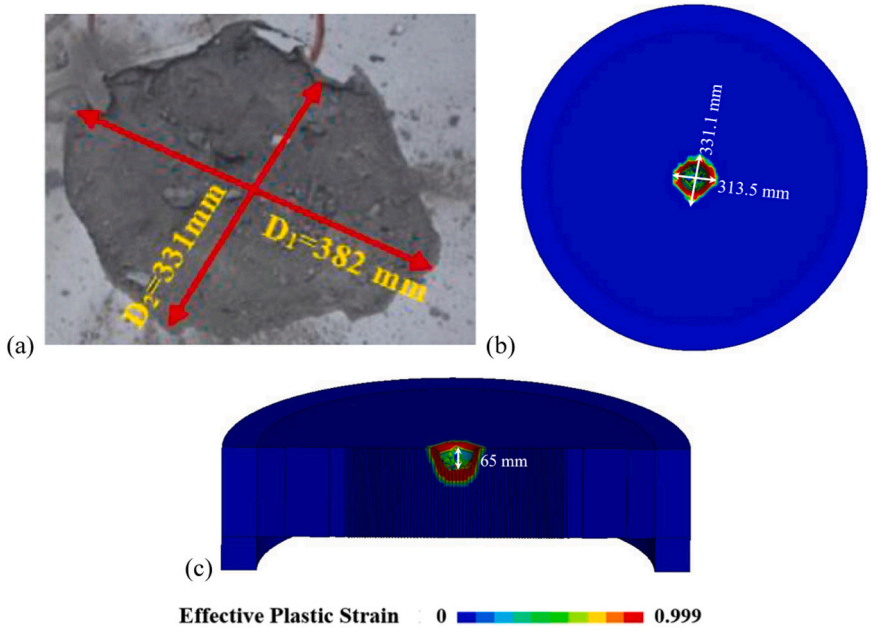


**Fig. 11.** Failure patterns of reinforced concrete panel for specimen 1. (a) Front crater from experiment (b) Front crater from numerical simulation (c) Penetration depth of concrete panel.

**Table 5**
Comparative analysis of numerical and experimental findings for concrete panels.

| Numerical Test Trial | Numerical results (mm) | | Experimental results (mm) | | Error (%) | |
|---|---|---|---|---|---|---|
| | Penetration depth | Equivalent diameter of crater | Penetration depth | Equivalent diameter of crater | Penetration depth | Equivalent diameter of crater |
| 1 | 65 | 322.2 | 57 | 356 | -14 | 9 |
| 2 | 102 | 333.5 | 103 | 357 | 1 | 7 |

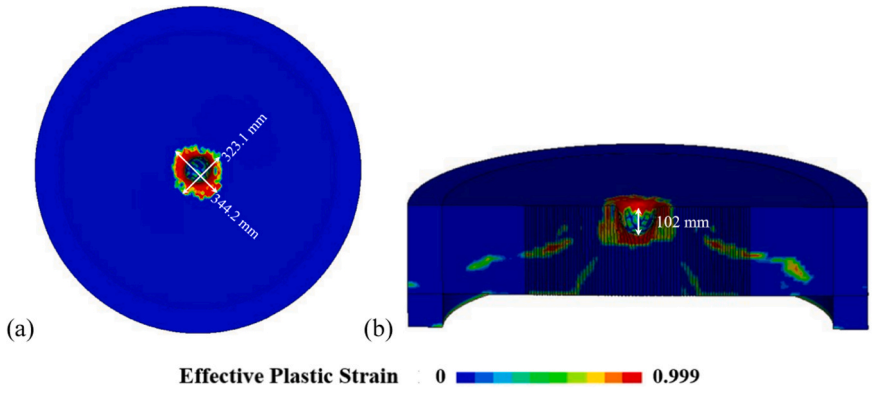


**Fig. 12.** Failure patterns of reinforced concrete panel for specimen 2. (a) Front crater from numerical simulation (b) Penetration depth of concrete panel.

the mass block was MAT_RIGID. Table 4 summarized the input parameters for each material.

AUTOMACITC_NODES_TO_SURFACE was utilised to model the contact between reinforcements and impactor, while keyword ERODING_SURFACE_TO_SURFACE was set for concrete and impactor. Besides, AUTOMATIC_SINGLE_SURFACE was adopted between concrete and steel liner. The consideration of reinforcement slippage was not included in the CONSTRAINED_BEAM_IN_SOLID keyword.

The failure patterns observed in the first specimen closely matched the experimental findings, which is evident from Fig. 11. $D_1$ and $D_2$ represented the maximum and minimum of the crater. The diameter of equivalent circle of the crater ($D_{eq}$) could be calculated as $\sqrt{D_1 D_2}$. Table 5 shows that the numerical prediction of $D_{eq}$ was 322.2 mm, while the experimental result measured 356 mm, resulting in an approximate difference of 9.5%. Furthermore, the penetration depth measured 65 mm in the numerical prediction, whereas the experimental result showed 57 mm, indicating an approximately 14.0% difference. Concerning specimen 2, the numerical prediction for $D_{eq}$ was 333.5 mm, while the experimental measurement recorded 357 mm, exhibiting an approximate difference of 6.6%. The penetration depth was predicted to be 102 mm in the numerical analysis, whereas the experimental data indicated 103 mm, resulting in an approximate difference of 0.97% (see Fig. 12). The results demonstrated a clear alignment between the numerical predictions and experimental measurements. As a result,

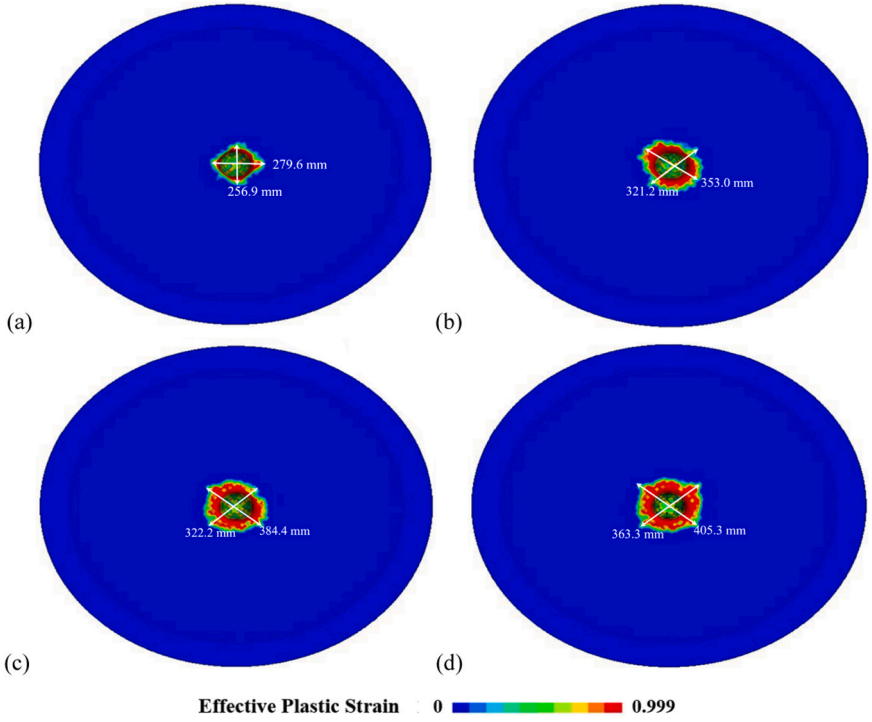


**Fig. 13.** Failure patterns of reinforced concrete panels. (a) 0 time FT cycle (b) 10 times FT cycles (c) 20 times FT cycles (d) 30 times FT cycles.

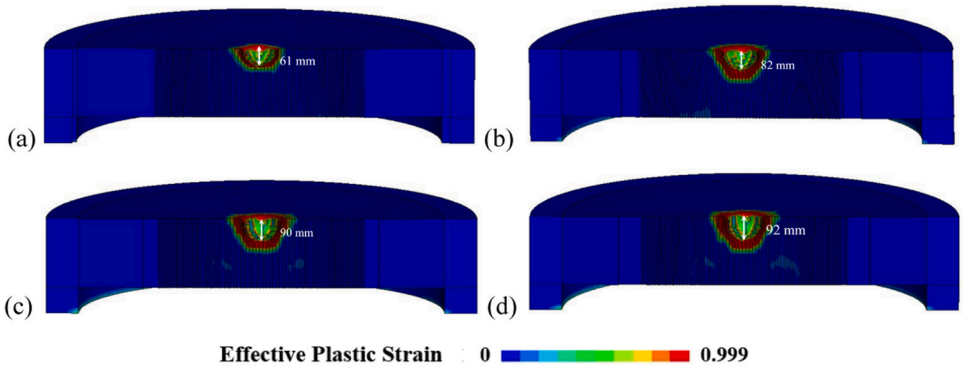


**Fig. 14.** Penetration depth of reinforced concrete panels. (a) 0 time FT cycle (b) 10 times FT cycles (c) 20 times FT cycles (d) 30 times FT cycles.

employing this numerical model allows for precise simulation of the impact behaviour observed in reinforced concrete panels subjected to FT cycles in subsequent studies.

## 4. Impact resistance of reinforced concrete panel after cryogenic FT cycles

In the preceding section, the material and numerical model validation demonstrated its capability to accurately forecast the impact resistance of the designated reinforced concrete panel under normal room temperature conditions. Nevertheless, when it comes to LNG storage tanks, the structural integrity faces an additional obstacle due to the effects of FT cycles. To analyse the influence of FT cycle in relation to reinforced concrete panel after cryogenic FT cycles, four different groups were tested, including 0 time, 10 times, 20 times and 30 times of FT cycles. The temperature ranged from 20 °C ~ − 165 °C with cooling rate 2–3 ℃/min. A 500 kg impactor was free-dropping at 35 m falling height (its impact velocity was 26.19 m/s). The dimension of the reinforced concrete panel was discussed in Section 3.2. In this section, the concrete compressive strength was set as 53.8 MPa. The MAT_CSCM_CONCRETE material model was utilized for analysing concrete without any exposure to FT cycles. Conversely, the MAT_CSCM model was employed to study the varying properties of NSC under various numbers of FT cycles, and the input parameters are summarised in Tables 1, 2 and 3. Other materials such as reinforcements, steel liner and impactor etc. were the same as those indicated in Section 3.2.

The failure patterns of target reinforced concrete panel are presented in Fig. 13. With an increase in the number of FT cycles, the dimensions of the crater on the upper surface of the target panel also expanded. $D_{eq}$ on the upper surface of the target panel for 0 time, 10 times, 20 times and 30 times of FT cycles was 268.0 mm, 336.7 mm, 351.9 mm and 383.7 mm, respectively. After 10 times, 20 times, as well as 30 times of FT cycles, the equivalent diameter of the crater was 1.25, 1.31 and 1.43 times greater than the specimen that had not undergone any FT cycles. This demonstrated a progressive enlargement of the front crater with each additional FT cycle. With the escalation in the number of FT cycles, there was a corresponding increase in the penetration depth of the target panel (see Fig. 14). Specifically, the penetration depth measurements for 0 time, 10 times, 20 times, and 30 times of FT cycles were 61 mm, 82 mm, 90 mm, and 93 mm, respectively. Additionally, after

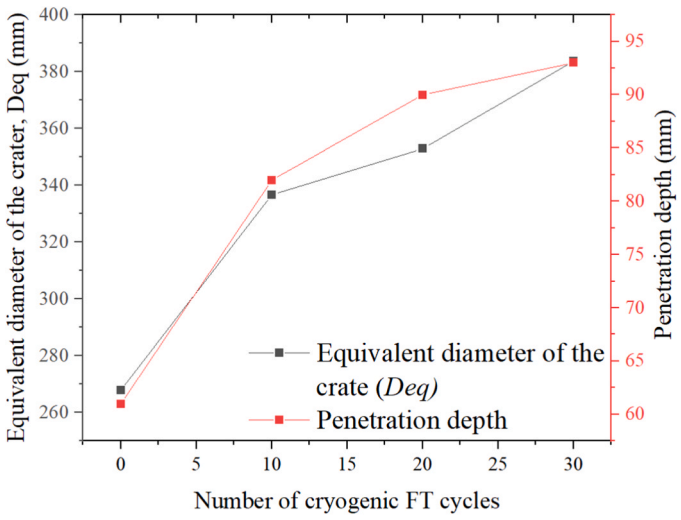


**Fig. 15.** Number of cryogenic FT cycles versus $D_{eq}$ and penetration depth.

undergoing 10 times, 20 times, and 30 times of FT cycles, the penetration depth increased by 1.34 times and 1.48 times as well as 1.52 times, respectively, as compared to the specimen that without any FT cycles. This indicated a clear and progressive amplification in the penetration depth as the number of FT cycles was augmented. In conclusion, the impact resistance of concrete structures could be influenced by FT cycles.

The repeated exposure to freezing and thawing conditions could lead to an increase in both the size of craters on the surface and the penetration depth (see Fig. 15). As the number of FT cycles rises, these effects become more pronounced, indicating that concrete structures, especially those subjected to harsh environmental conditions, may experience reduced impact resistance over time. From Section 2, it was evident that this phenomenon was related to the decrease in concrete performance such as compressive strength, splitting tensile strength, fracture energy etc. after cryogenic FT cycles. This degradation in impact resistance is a critical consideration for the long-term durability and performance of such structures, warranting careful assessment and appropriate mitigation strategies in design and maintenance practices.

## 5. Parametric study

Utilizing the aforementioned model, a parametric study was conducted to examine the impact behaviour of target concrete panels under both ambient temperature conditions and after undergoing FT cycles. This study aimed to investigate the effects of various parameters on the panel's response. The mesh size and material model were identical to those in Section 4. In this section, it would explore the influence of impact velocity and impact mass at ambient temperature and after 10 times of cryogenic FT cycles.

### 5.1. Effect of impact velocity

To assess the effect of varying impact velocities on reinforced concrete panels after undergoing FT cycles, four distinct impact velocity groups were examined. These groups included impact velocities of 19.70 m/s (corresponding to a falling height of 20 m), 22.13 m/s (dropping height of 25 m), and 24.24 m/s (dropping height of 30 m), as well as 26.19 m/s (dropping height of 35 m). A 500 kg weight was used as the impactor during the tests. Fig. 16 shows the failure patterns of reinforced concrete panels at ambient temperature under different impact velocities. The diameter of the equivalent circle of the crater with falling height 20 m, 25 m and 30 m was 191.1 mm, 221.3 mm and

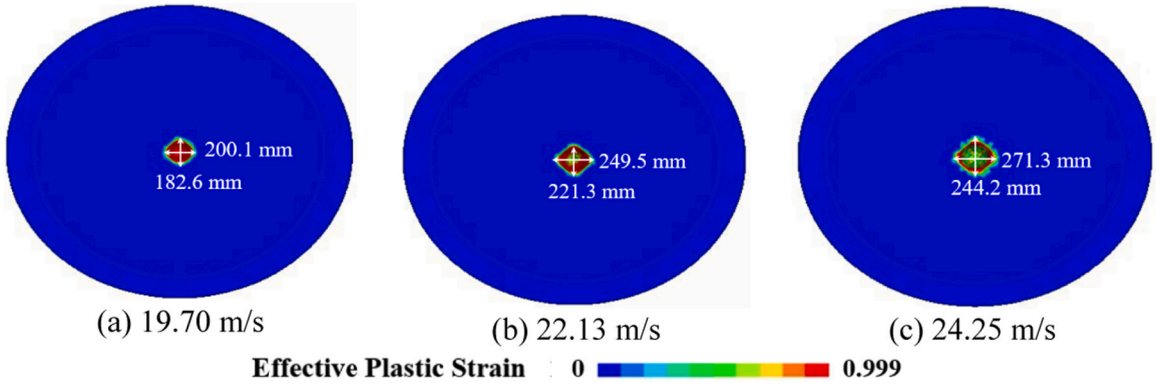


**Fig. 16.** Final damage patterns of target panels at different impact velocities at ambient temperature.

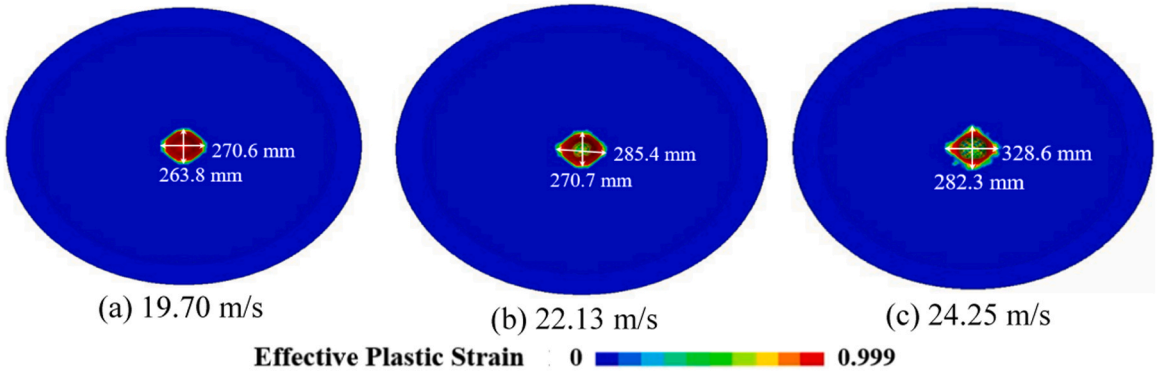


**Fig. 17.** Final damage patterns of target panels at different impact velocities after 10 FT cycles.

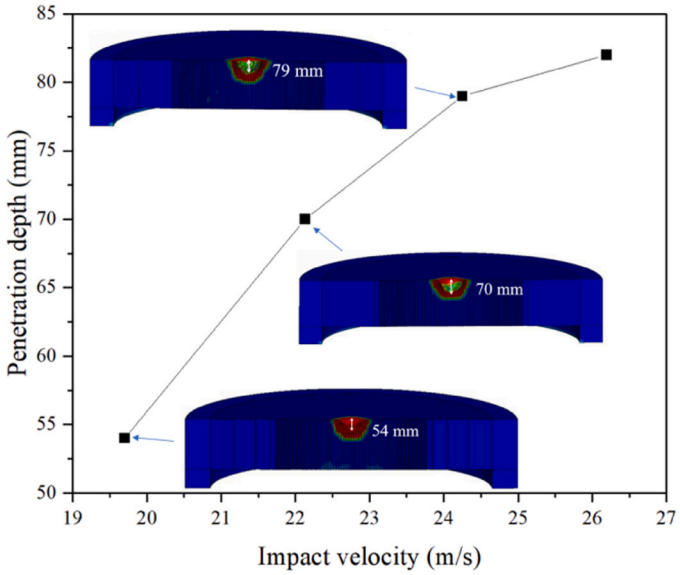


**Fig. 18.** Penetration depth of target panels in different impact velocities.

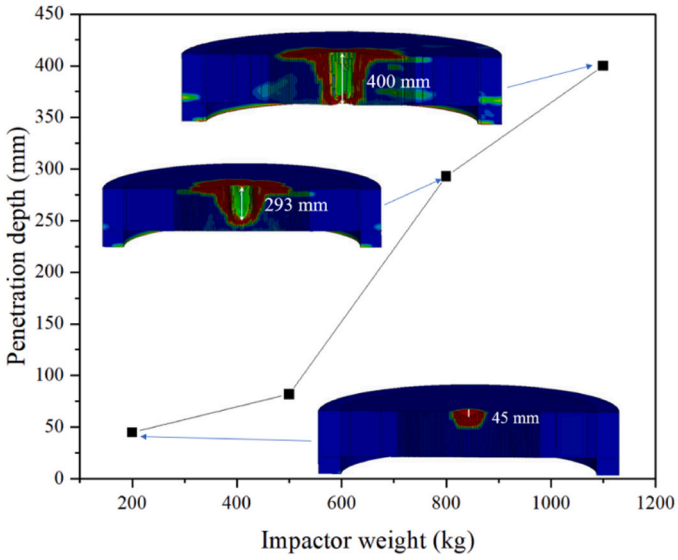


**Fig. 21.** Penetration depth of target panels in different impact mass.

257.4 mm and the penetration depth was 51 mm, 55 mm, and 60 mm, respectively. Fig. 17 displays the final damage patterns of the target panels under various impact velocities after 10 FT cycles, similar to ambient condition, higher impact velocities led to more severe damage on the panels. The diameter of the equivalent circle of the crater at the same impact velocities of 19.70, 22.13 and 24.24 m/s was measured at 267.2 mm, 278.0 mm, and 304.6 mm, respectively. It was clear that the target panels at ambient temperature are more impact resistant than those after 10 FT cycles.

Unsurprisingly, as the impact velocity increased, a greater penetration depth of the panel was observed, as demonstrated in Fig. 18. At impact velocities of 19.70, 22.13 and 24.24 m/s, the penetration depths

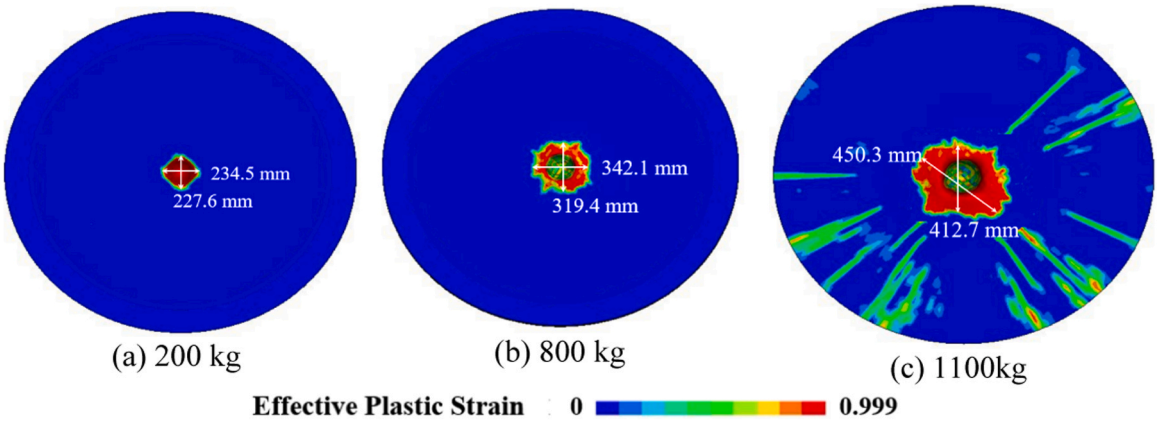


**Fig. 19.** Final damage patterns of target panels in different impact weights at ambient temperature.

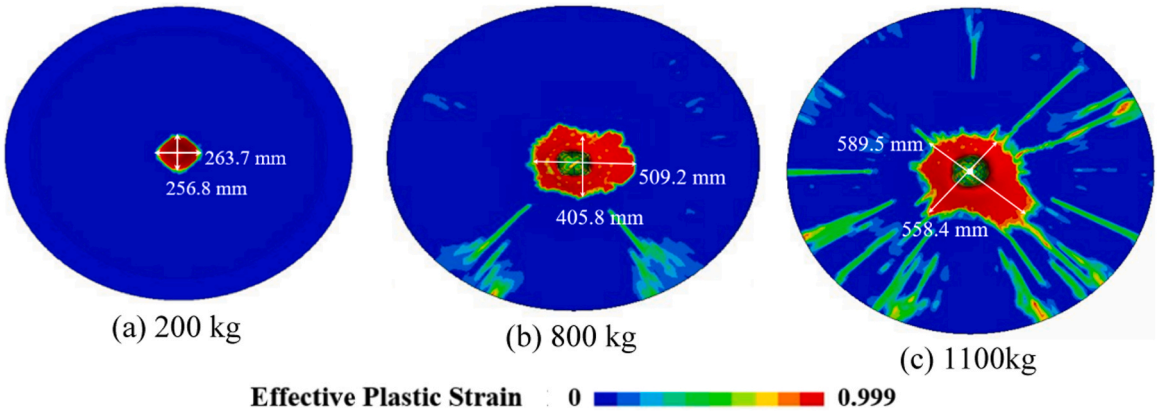


**Fig. 20.** Final damage patterns of target panels in different impact weights after 10 FT cycle.

were measured as 54 mm, 70 mm, and 74 mm, respectively. This indicates that higher impact velocities are associated with deeper penetration into the panel. With an equivalent impact weight, it was evident that the impact resistance of concrete panels following 10 FT cycles was inferior as compared to their performance at room temperature.

### 5.2. Effect of impactor weight

The effect of impactor weight was examined by altering the weight of the punch utilized in the tests to 200, 500, and 800 as well as 1100 kg. The falling height was kept constant at 35 m, resulting in an impact velocity of 26.19 m/s during the experiments. Fig. 19 displays the failure patterns of reinforced concrete panels at ambient temperature under different impactor mass. The diameter of the equivalent circle of the crater with impactor mass 200, 800 and 1100 kg was 231.1 mm, 330.6 mm and 431.1 mm and the penetration depth was 42 mm, 273 mm and 400 mm, respectively. Based on the damage level from Zou *et al.* [49], damage level I refers to the formation of a localized crater solely on the front surface of the reinforced concrete panel upon impact; Damage level II involves not only the presence of a front impact crater but also the emergence and propagation of both radial and circumferential cracks; Damage level III is characterized by the complete perforation of the reinforced concrete (RC) panel, signifying a severe level of structural damage where the panel has been entirely penetrated. Compared with 200 and 800 kg, circumferential and radial cracks were developed in the target concrete panel with 1100 kg, which referred to damage level II. Furthermore, the punching shear failure area increase dramatically with the increase of impact mass. Fig. 20 presents the final damage patterns of the target panels under different impact masses subjected to 10 cycles of FT, indicating that higher impact masses resulted in more severe damage to the panels. Notably, when the impact weight reached 1100 kg, the hammer penetrated the entire concrete panel. The diameter of the equivalent circle of the crater at impact masses of 200, 800, and 1100 kg was measured as 260.2 mm, 454.6 mm, and 573.5 mm, respectively. From Fig. 20 (c), it could be observed that the entire target plate was punctured by a high-speed punch, resulting in circumferential and radial cracks. This was the most severe specimen among all tests, which was damage level III. It was significant to highlight that, in Fig. 18 and Fig. 19, the diameter of the equivalent circle of the crater on the panel after 10 cycles of FT, demonstrated increments of 1.1 times, 1.3 times, 1.4 times, and 1.3 times in comparison to the panels subjected to ambient temperature conditions, respectively.

Additionally, as illustrated in Fig. 21, an increase in impact mass led to a greater penetration depth of the panel. Specifically, the penetration depth for impact masses of 200, 800, and 1100 kg was measured as 45 mm, 293 mm, and 400 mm, respectively. The penetration depth for 500, 800 and 1100 kg impactor was 1.82 times, 6.5 times, and 8.89 times greater than the 200 kg one. It was noted that the impact resistance of concrete panels exhibited a decline following 10 FT cycles, in contrast to its performance under room temperature conditions at the same impact velocity.

## 6. Limitations

The current study specifically targets at the impact resistance of reinforced concrete structures, particularly in scenarios involving cryogenic FT cycles. This model is closely related to critical energy infrastructure applications, such as ACLNG storage tanks.

Notwithstanding its contributions, this study does have certain limitations. The reliance on numerical simulation for predicting the impact resistance of the concrete slab after FT cycles might not capture all real-world complexities. The current study is limited to a typical concrete material with uniaxial compressive strength of 53.8 MPa and a water-to-cement (w/c) ratio of 0.44. Variations in material properties, such as compressive strength and w/c ratio, could yield different outcomes, and therefore, the generalization of the findings to a broader range of concrete compositions may require further experimental investigation and validation. In addition, further physical tests are deemed necessary especially the triaxial material strength and structural impact behaviour under FT cycles, which can further help understand the impact resistance performance of concrete slabs after FT cycles.

## 7. Conclusions

The impact resistance of reinforced NSC panels after FT cycles was investigated using a refined finite element model. The CSCM model was adopted and modified to incorporate various parameters such as shear modulus ($G$), bulk modulus ($K$), uniaxial and triaxial compression surface, as well as damage parameters. The subsequent conclusions can be drawn:

- After FT cycles, the elastic modulus, splitting tensile, and compressive strength as well as fracture energy of concrete decrease. As the number of FT cycles increases, the performance of concrete also continuously decreases.
- The modified CSCM model effectively captures the impact behaviour of reinforced concrete panels after FT cycles, considering various mechanical parameters.
- The predictive capability of the numerical model was validated through experimental verification, demonstrating its reliability in assessing the impact resistance of reinforced concrete structures.
- FT cycles were observed to adversely affect the impact resistance of the concrete structures. As the number of FT cycles increased, there was an observable escalation in the dimensions of craters formed on the surface as well as an increase in the penetration depth of the panels. These trends collectively suggested a decline in the impact resistance of the panels with the progression of FT cycles.

## CRediT authorship contribution statement

**Chi Kaiyi:** Writing – original draft, Investigation. **Wu Chengqing:** Writing – review & editing, Funding acquisition, Conceptualization. **Li Jun:** Writing – review & editing, Supervision, Investigation, Formal analysis, Conceptualization.

## Declaration of Competing Interest

The authors declare that there is no conflict of interest.

## Data availability

Data will be made available on request.

## Acknowledgements

This work was supported by ARC LP220200796 and DP210101100 are supporting this research.

## Appendix. Alterations in concrete characteristics subsequent to FT cycles in comparison to no FT cycles

| | References | Temperature range | W/C | Moisture Content (%) | Thermal Cycles | | | | | | | | | | | | | | |
|---|---|---|---|---|---|---|---|---|---|---|---|---|---|---|---|---|---|---|---|
| | | | | | 0 | 1 | 2 | 3 | 4 | 5 | 6 | 8 | 10 | 12 | 14 | 15 | 16 | 20 | 25 | 30 |
| Compressive strength | Van de Veen [8] | 20 ℃ ~ − 170 ℃ | 0.54 | water saturated | 1 | 0.75 | 0.79 | \ | 0.63 | \ | 0.65 | 0.58 | \ | 0.5 | \ | \ | \ | \ | \ | \ |
| | | 20 ℃ ~ − 170 ℃ | 0.54 | water saturated | 1 | 0.81 | 0.82 | \ | 0.7 | \ | 0.65 | 0.59 | \ | 0.51 | \ | \ | \ | \ | | \ |
| | Lee et al. [13] | 8 °C ~ − 52 °C | 0.48 | \ | 1 | 0.98 | \ | \ | \ | \ | \ | \ | 0.95 | \ | \ | \ | \ | \ | \ | 0.95 |
| | Rostásy and Punch [14] | 20 °C ~ − 85 °C | 0.5 | 7.2 | 1 | 0.92 | \ | 0.99 | \ | \ | \ | \ | 0.97 | \ | \ | \ | \ | \ | \ | \ |
| | | | 0.5 | 11.1 | 1 | 0.89 | \ | 0.86 | \ | \ | \ | \ | 0.61 | \ | \ | \ | \ | \ | \ | \ |
| | | | 0.49 | 7.3 | 1 | 1 | \ | 1.1 | \ | \ | \ | \ | 0.96 | \ | \ | \ | \ | \ | \ | \ |
| | | | 0.52 | 13.4 | 1 | 0.95 | \ | 0.86 | \ | \ | \ | \ | 0.62 | \ | \ | \ | \ | \ | \ | \ |
| | Rostásy *et al.* [15] | 20 °C ~ − 170 °C | 0.54 | water saturated | 1 | 0.85 | \ | \ | 0.65 | \ | \ | \ | \ | \ | \ | \ | \ | \ | \ | \ |
| | Kim et al. [16] | 15 °C ~ − 190 °C | 0.47 | \ | 1 | 0.96 | \ | \ | \ | | \ | \ | \ | \ | \ | \ | \ | \ | \ | \ |
| | Shi et al. [20] | 15 °C ~ − 120 °C | 0.57 | \ | 1 | \ | \ | \ | \ | \ | \ | \ | \ | \ | \ | \ | 0.75 | \ | \ | 0.7 |
| | | 15 °C ~ − 190 °C | 0.57 | \ | 1 | \ | \ | \ | \ | \ | \ | \ | \ | \ | \ | \ | 0.7 | \ | \ | 0.8 |
| | Zhou et al. [21] | 20 °C ~ − 165 °C | 0.44 | \ | 1 | \ | \ | \ | \ | \ | \ | \ | 0.842 | \ | \ | \ | \ | 0.786 | \ | 0.75 |
| | Xie and Wu [40] | 20 ℃ ~ − 160 ℃ | 0.4 | \ | 1 | \ | \ | 0.9 | \ | \ | \ | \ | \ | \ | \ | \ | \ | \ | \ | \ |
| | | 20 ℃ ~ − 160 ℃ | 0.25 | \ | 1 | \ | \ | 0.92 | \ | \ | \ | \ | \ | \ | \ | \ | \ | \ | \ | \ |
| | Wei et al. [42] | 20 ℃ ~ − 160 ℃ | 0.23 | \ | 1 | \ | \ | 0.9 | \ | \ | \ | \ | \ | \ | \ | \ | \ | \ | \ | \ |
| Splitting tensile strength | Van de Veen [8] | 20 ℃ ~ − 170 ℃ | 0.54 | water saturated | 1 | 0.69 | 0.63 | \ | 0.42 | \ | 0.5 | 0.3 | \ | 0.21 | \ | \ | \ | \ | \ | \ |
| | | 20 ℃ ~ − 170 ℃ | 0.54 | water saturated | 1 | 0.7 | 0.73 | \ | 0.58 | \ | 0.59 | 0.58 | \ | 0.58 | \ | \ | \ | \ | | \ |
| | Rostásy and Punch [14] | 20 °C ~ − 85 °C | 0.5 | 7.2 | 1 | 1.17 | \ | 1.1 | \ | \ | \ | \ | 1.01 | \ | \ | \ | \ | \ | \ | \ |
| | | | 0.5 | 11.1 | 1 | 0.89 | \ | 0.9 | \ | \ | \ | \ | 0.54 | \ | \ | \ | \ | \ | \ | \ |
| | | | 0.49 | 7.3 | 1 | 0.9 | \ | 0.81 | \ | \ | \ | \ | 0.805 | \ | \ | \ | \ | \ | \ | \ |
| | | | 0.52 | 13.4 | 1 | 0.8 | \ | 0.6 | \ | \ | \ | \ | 0.43 | \ | \ | \ | \ | \ | \ | \ |
| | Rostásy et al. [15] | 20 °C ~ − 170 °C | 0.54 | water saturated | 1 | 0.7 | \ | \ | 0.5 | \ | \ | \ | \ | \ | \ | \ | \ | \ | \ | \ |
| | Kim et al. [16] | 20 °C ~ − 170 °C | 0.47 | \ | 1 | 0.91 | \ | \ | \ | \ | \ | \ | \ | \ | \ | \ | \ | \ | \ | \ |
| | Xie and Wu [40] | 20 ℃ ~ − 160 ℃ | 0.25 | water saturated | 1 | \ | \ | 0.88 | \ | \ | \ | \ | \ | \ | \ | \ | \ | \ | \ | \ |
| | | 20 ℃ ~ − 160 ℃ | 0.23 | water saturated | 1 | \ | \ | 0.8 | \ | \ | \ | \ | \ | \ | \ | \ | \ | \ | \ | \ |
| | Liu et al. [41] | 20 °C ~ − 160 °C | 0.36 | \ | 1 | 0.7 | \ | \ | \ | \ | \ | \ | \ | \ | \ | \ | \ | \ | \ | \ |
| | | 20 °C ~ − 200 °C | 0.36 | \ | 1 | 0.6 | \ | \ | \ | \ | \ | \ | \ | \ | \ | \ | \ | \ | \ | \ |

(*continued on next page*)

(*continued*)

| | References | Temperature range | W/C | Moisture Content (%) | Thermal Cycles | | | | | | | | | | | | | | | |
|---|---|---|---|---|---|---|---|---|---|---|---|---|---|---|---|---|---|---|---|---|
| | | | | | 0 | 1 | 2 | 3 | 4 | 5 | 6 | 8 | 10 | 12 | 14 | 15 | 16 | 20 | 25 | 30 |
| | Berner and Gerwick [39] | 21 ℃ ~ − 196 ℃ | 0.35 | air dry (non-air entrained) | 1 | 0.98 | 0.9 | 0.75 | 0.6 | 0.56 | 0.5 | | \ | \ | \ | \ | \ | \ | \ | \ |
| | | 21 ℃ ~ − 196 ℃ | 0.35 | air dry (air entrained) | 1 | 0.95 | 0.82 | 0.78 | 0.58 | 0.5 | 0.3 | | \ | \ | \ | \ | \ | \ | \ | \ |
| Modulus of Elasticity | Lee et al. [13] | 8 °C ~ − 52 °C | 0.48 | \ | 1 | 1 | \ | \ | \ | \ | | \ | 0.948 | \ | | \ | \ | \ | \ | 0.91 |
| | Shi et al. [18] | -30 °C ~ − 120 °C | 0.5 | 4.62 | 1 | 1.11 | 0.85 | \ | 0.83 | \ | 0.96 | 0.79 | 0.79 | \ | \ | \ | \ | \ | \ | \ |
| | | 20 °C ~ − 120 °C | 0.5 | 4.62 | 1 | 0.98 | 1.03 | \ | 0.97 | \ | \ | 0.87 | 0.73 | 0.77 | 0.87 | \ | 0.8 | \ | \ | |
| | Shi et al. [19] | 10 °C ~ − 40 °C | 0.51 | \ | 1 | 0.94 | \ | 1.05 | \ | \ | 0.91 | \ | 0.81 | \ | \ | 0.89 | \ | \ | \ | \ |
| | | 10 °C ~ − 160 °C | 0.49 | \ | 1 | \ | \ | \ | \ | \ | \ | \ | 1.18 | \ | \ | 1.01 | \ | 0.98 | 0.86 | 0.73 |
| | Goto and Miura [35] | 20 °C ~ − 196 °C | 0.26 | water saturated | 1 | 0.98 | 0.96 | 0.95 | 0.96 | 0.81 | 0.79 | 0.6 | 0.5 | \ | \ | \ | \ | \ | \ | \ |
| | | | 0.36 | water saturated | 1 | 0.97 | 0.9 | 0.87 | 0.9 | 0.82 | 0.57 | \ | \ | \ | \ | \ | \ | \ | \ | \ |
| | | | 0.46 | water saturated | 1 | 0.9 | 0.7 | 0.61 | 0.58 | \ | \ | \ | \ | \ | \ | \ | \ | \ | \ | \ |
| | | | 0.36 | 4.96 | 1 | | 0.9 | \ | 0.87 | \ | 0.65 | 0.59 | \ | \ | \ | \ | \ | \ | \ | \ |
| | | | 0.36 | 4.57 | 1 | \ | 0.93 | \ | 0.94 | \ | 0.93 | 0.932 | 0.932 | 0.926 | 0.924 | \ | 0.926 | 0.92 | \ | 0.79 |
| | | | 0.36 | 4.33 | 1 | \ | 0.93 | \ | 0.94 | \ | 0.93 | 0.933 | 0.933 | 0.927 | 0.926 | | 0.928 | 0.928 | \ | 0.82 |
| | | | 0.36 | 3.71 | 1 | \ | 0.93 | \ | 0.95 | \ | 0.93 | 0.935 | 0.915 | 0.936 | 0.933 | \ | 0.938 | 0.928 | \ | 0.87 |
| | Yamane et al. [36] | 20 °C ~ − 196 °C | 0.5 | water saturated | 1 | 0.5 | \ | 0.18 | \ | \ | \ | \ | \ | \ | \ | \ | \ | \ | \ | \ |
| | | | 0.61 | water saturated | 1 | 0.29 | \ | 0.09 | \ | \ | \ | \ | | \ | \ | \ | \ | \ | \ | \ |
| | Rostasy and Wiedemann [37] | 20 °C ~ − 170 °C | 0.5 | water saturated | 1 | \ | \ | \ | \ | \ | \ | 0.35 | \ | \ | \ | \ | \ | \ | \ | \ |
| | | | 0.55 | water saturated | 1 | \ | | \ | \ | \ | \ | 0.22 | \ | \ | \ | \ | \ | \ | \ | \ |
| | | | 0.6 | water saturated | 1 | \ | \ | \ | \ | \ | \ | 0.16 | \ | \ | \ | \ | \ | \ | \ | \ |
| | | | 0.65 | water saturated | 1 | | \ | \ | \ | \ | \ | 0.13 | \ | \ | \ | \ | \ | \ | \ | \ |
| | | | 0.7 | water saturated | 1 | \ | \ | \ | \ | \ | \ | 0.11 | \ | \ | \ | \ | \ | | \ | \ |
| Fracture energy | Xie et al. [26] | 20 °C ~ − 80 °C | 0.82 | \ | 1 | \ | \ | \ | | 0.81 | \ | \ | 0.71 | \ | \ | \ | \ | \ | \ | \ |
| | | 20 °C ~ − 80 °C | 0.5 | \ | 1 | \ | \ | \ | \ | 0.86 | \ | \ | 0.81 | \ | \ | \ | \ | \ | \ | \ |
| | | 20 °C ~ − 80 °C | 0.36 | \ | 1 | \ | \ | \ | \ | 0.77 | \ | \ | 0.7 | \ | \ | \ | \ | \ | \ | \ |
| Bond strength | Lee et al. [13] | 20 °C ~ − 70 °C | 0.48 | \ | 1 | 0.99 | \ | \ | \ | \ | \ | \ | 0.975 | \ | \ | \ | \ | \ | \ | 0.92 |
| | Xie et al. [30] | 20 °C ~ − 40 °C | 0.36 | \ | 1 | \ | \ | 0.94 | \ | \ | \ | \ | \ | \ | \ | \ | \ | \ | \ | \ |
| | | 20 °C ~ − 75 °C | 0.36 | \ | 1 | \ | \ | 0.87 | \ | 0.86 | \ | \ | \ | \ | \ | \ | \ | \ | \ | \ |
| | | 20 °C ~ − 120 °C | 0.36 | \ | 1 | \ | \ | 0.86 | \ | 0.81 | \ | \ | \ | \ | \ | | \ | \ | \ | \ |

## References


[1] N. Krstulovic-Opara, Liquefied natural gas storage: Material behavior of concrete at cryogenic temperatures, Acids Mater. J. 104 (3) (2007) 297.
[2] R.B. Kogbara, S.R. Iyengar, Z.C. Grasley, E.A. Masad, D.G. Zollinger, A review of concrete properties at cryogenic temperatures: Towards direct LNG containment, Constr. Build. Mater. 47 (2013) 760–770.
[3] Monfore, G. and A. Lentz, *Physical properties of concrete at very low temperatures*. 1962.
[4] Goto, Y. and T. Miura. *Mechanical properties of concrete at very low temperatures*. in Proceedings of 21st Japan Congress on Materials Research. 1978. The Society of Materials Science Japan.
[5] MITSUI, K., T. YONEZAWA, and I. TAKAYUKI, *Mechanical Properties of High Strength Concreteunder Cryogenic At-mosphere.* Proceedings of the Japan Concrete Institute (in Janpanese), 1997. **19**(1): p. 175–180.
[6] H. Lin, Y. Han, S. Liang, F. Gong, S. Han, C. Shi, P. Feng, Effects of low temperatures and cryogenic freeze-thaw cycles on concrete mechanical properties: a literature review, Constr. Build. Mater. 345 (2022) 128287.
[7] Y. Huo, H. Sun, D. Lu, Z. Chen, Y. Yang, Mechanical properties of concrete at low and ultra-low temperatures-a review, J. Infrastruct. Preserv. Resil. 3 (1) (2022) 1–15.
[8] V. Van de Veen, Properties of concrete at very low temperatures: a survey of the literature. Report Stevin, -2, Lab. Concr. Struct. (1987) 25–87. -2.
[9] L. Dahmani, A. Khenane, S. Kaci, Behavior of the reinforced concrete at cryogenic temperatures, Cryogenics 47 (9-10) (2007) 517–525.
[10] J. Xie, J. Yan, Experimental studies and analysis on compressive strength of normal-weight concrete at low temperatures, Struct. Concr. 19 (4) (2018) 1235–1244.
[11] F. Gong, Y. Wang, T. Ueda, D. Zhang, Modeling and mesoscale simulation of ice-strengthened mechanical properties of concrete at low temperatures, J. Eng. Mech. 143 (6) (2017) 04017022.
[12] F. Gong, T. Ueda, D. Zhang, Two-dimensional rigid body spring method based micro-mesoscale study of mechanical strengthening/damaging effects to concrete by frost action, Struct. Concr. 19 (4) (2018) 1131–1145.
[13] G. Lee, T. Shih, K.-C. Chang, Mechanical properties of concrete at low temperature, J. Cold Reg. Eng. 2 (1) (1988) 13–24.
[14] F. Rostásy, U. Pusch, Strength and deformation of lightweight concrete of variable moisture content at very low temperatures, Int. J. Cem. Compos. Lightweight Concr. 9 (1) (1987) 3–17.
[15] F. Rostasy, U. Schneider, G. Wiedemann, Behaviour of mortar and concrete at extremely low temperatures, Cem. Concr. Res. 9 (3) (1979) 365–376.
[16] M.-J. Kim, S. Kim, S.-K. Lee, J.-H. Kim, K. Lee, D.-Y. Yoo, Mechanical properties of ultra-high-performance fiber-reinforced concrete at cryogenic temperatures, Constr. Build. Mater. 157 (2017) 498–508.
[17] X. Shi, W. Wang, L. Qian, J.L. Li, Experimental study on compressive strength of concrete with different water content experiencing cryogenic freeze-thaw cycles from room temperature to-190℃, Cryogenics 2 (2017) 17–22.
[18] X. Shi, J. Li, W. Wang, L. Qian, C. Ma, Experimental study on stress-strain relationships of concrete undergoing cryogenic freeze-thaw cycles from room temperature or -30℃ to -120℃, Concrete 12 (2017) 1–5.
[19] X. Shi, Y. LI, L. QIAN, J. LI, W. WANG, Experimental study on elastic modulus of concrete undergoing freeze-thaw cycle action with different ultralow temperature ranges, Eng. Mech. 36 (8) (2019) 106–113.
[20] X. Shi, W. Wang, J. Tian, Experimental study on the compressive strength of concrete of different strength grades experiencing ultralow temperature freeze-thaw cycle action, Eng. Mech. 37 (2) (2020) 211–220.
[21] D. Zhou, J. Liu, P. Duan, L. Cheng, B. Lou, Damage evolution law an mechanism of concrete under cryogenic freeze-thaw cycles, J. Build. Mater. (2021) 1–13.
[22] M. Sun, D. Xin, C. Zou, Damage evolution and plasticity development of concrete materials subjected to freeze-thaw during the load process, Mech. Mater. 139 (2019) 103192.
[23] U. Ohlsson, P.A. Daerga, L. Elfgren, Fracture energy and fatigue strength of unreinforced concrete beams at normal and low temperatures, Eng. Fract. Mech. 35 (1-3) (1990) 195–203.
[24] P. Maturana, J. Planas, M. Elices, Evolution of fracture behaviour of saturated concrete in the low temperature range, Eng. Fract. Mech. 35 (4-5) (1990) 827–834.
[25] Rocco, C., J. Planas, G. Guinea, and M. Elices, Fracture properties of concrete under cryogenic conditions. Borst et al.(eds) pp, 2001: p. 1–8.
[26] J. Xie, M. YAN, Y. LIU, Effect of freezing and thawing on fracture performance of concrete at polar low temperature, Eng. Mech. 39 (2021) 1–11.
[27] L. Vandewalle, Bond between a reinforcement bar and concrete at normal and cryogenic temperatures, J. Mater. Sci. Lett. 8 (2) (1989) 147–149.
[28] L. Jin, K. Liu, R. Zhang, W. Yu, X. Du, Bond behavior between steel bar and concrete considering cryogenic temperatures and confinement, Case Stud. Constr. Mater. 18 (2023) e01856.
[29] R. Zhang, K. Liu, L. Jin, W. Yu, X. Du, Bond-slip behavior between deformed rebar and concrete at cryogenic temperatures, J. Mater. Civ. Eng. 35 (10) (2023) 04023356.
[30] J. Xie, Q. Wei, H.L.I. Bonding, properties between reinforcement and concrete after freeze-thaw cycles at extra-low temperatures, J. Tianjing Univ. 46 (2013) 1012–1018.
[31] Liu, S., X. Gu, Q. Huang, and W. Zhang, Experimental study on the bending behavior of reinforced concrete beams under super-low temperature, in Earth and Space 2010: Engineering, Science, Construction, and Operations in Challenging Environments. 2010. p. 3537–3544.
[32] J. Yan, J. Xie, Behaviours of reinforced concrete beams under low temperatures, Constr. Build. Mater. 141 (2017) 410–425.
[33] C.E.-Id Béton, CEB-FIP model code 1990: Design code, Thomas Telford Publishing, 1993.
[34] Murray, Y.D., Users manual for LS-DYNA concrete material model 159. 2007, United States. Federal Highway Administration. Office of Research ….
[35] Y. Goto, T. Miura, Deterioration of concrete subjected to repetitions of very low temperatures, Transactions of the Japan Concrete Institute, 1979, pp. 183–190.
[36] S. Yamane, H. Kasami, T. Okuno, Properties of concrete at very low temperatures, 55, Special Publication, 1978, pp. 207–222.
[37] Rostasy, F.S. and G. Wiedemann, Strength and deformability of concrete after low temperature cycles. Proceedings, Second International Conference on Cryogenic Concrete, Amsterdam 1983. 8 pp.
[38] Kornen Hallgeir, J.H. Andersen, Properties of cryogenic concrete, The Nordic Concrete Federation, Oslo, 1983, pp. 149–165.
[39] Berner, D.E. and B. Gerwick. Static and cyclic behavior of structural lightweight concrete at cryogenic temperatures. in Ocean Space Utilization'85: Proceedings of the International Symposium Nihon University, Tokyo, Japan, June 1985 Volume 2. 1985. Springer.
[40] J. Xie, H. Wu, Experimental research on concrete strength under freeze–thaw recycle action with ultra-low temperature, J. Civ. Archit. Environ. Eng. 34 (2012) 165–168.
[41] j Liu, H. Liang, M. Han, X. Shi, Y. Cui, Experimental study on tensile strength of concrete subjected to differenet ultra low temperatures and returning to room temperature, Spec. Struct. 38 (6) (2021) 8–14.
[42] Q. Wei, J. Xie, H. Wu, Experimental analysis on properties of concrete after freeze-thaw cycles under extra-low temperatures, Eng. Mech. 30 (2013) 125–131.
[43] Australia, S., *AS 3600:2018- Australian Standard for Concrete Structures*, in *BD-002: Concrete Structures, Sydney* . 2018.
[44] X. Yin, Q. Li, X. Xu, B. Chen, K. Guo, S. Xu, Investigation of continuous surface cap model (CSCM) for numerical simulation of strain-hardening fibre-reinforced cementitious composites against low-velocity impacts, Compos. Struct. 304 (2023) 116424.
[45] Wu, Y., J.E. Crawford, and J.M. Magallanes. Performance of LS-DYNA concrete constitutive models. in 12th International LS-DYNA users conference. 2012.
[46] J.-B. Yan, J. Xie, Experimental studies on mechanical properties of steel reinforcements under cryogenic temperatures, Constr. Build. Mater. 151 (2017) 661–672.
[47] J. Xie, R. Xi, C. Tong, J.-B. Yan, Mechanical properties of Q235~ Q460 mild steels at low temperatures, Constr. Build. Mater. 363 (2023) 129850.
[48] D.-H. Jung, J.-K. Kwon, N.-S. Woo, Y.-J. Kim, M. Goto, S. Kim, S–N fatigue and fatigue crack propagation behaviors of X80 steel at room and low temperatures, Metall. Mater. Trans. A 45 (2014) 654–662.
[49] D. Zou, J. Sun, H. Wu, Y. Hao, Z. Wang, L. Cui, Experimental and numerical studies on the impact resistance of large-scale liquefied natural gas (LNG) storage outer tank against the accidental missile, Thin-Walled Struct. 158 (2021) 107189.